Protein Dynamics and Its Prediction Using Machine Learning

Oleg Trott

Submitted in partial fulfillment of the requirements for the degree of Doctor of Philosophy in the Graduate School of Arts and Sciences

COLUMBIA UNIVERSITY

2004

Contents

Abstract

In the first part of this dissertation, chemical exchange and the use of $R_{1\rho}$ rotating frame relaxation experiment for its study are discussed. Beginning with the Bloch-McConnell equations, new expressions are derived for the spin relaxation rate constant in the rotating frame, $R_{1\rho}$, for chemical exchange between two or more sites that have distinct magnetic environments and Larmor frequencies. The 2-site results are accurate provided that the spin relaxation decay is dominated by a single exponential damping constant and are applicable to a wider range of conditions than existing theoretical descriptions. The n-site results are accurate when the population of one of the sites is much greater than that of others.

The second part of this dissertation discusses the prediction of protein backbone flexibility using machine learning. Using a data set of 16 proteins, a neural network has been trained to predict backbone ^{15}N generalized order parameters from the three-dimensional structures of proteins. The average prediction accuracy, as measured by the Pearson correlation coefficient between experimental and predicted values of the square of the generalized order parameter is 71.4%. The network parameterization contains six input features. Predicted order parameters for non-terminal amino acid residues depends most strongly on local packing density and the probability that the residue is located in regular secondary structure.

Acknowledgements

My adviser, Arthur Palmer (Columbia University) took an active part in the work described here. Some of the results pertaining $R_{1\rho}$ relaxation are a product of our collaboration with Daniel Abergel (Ecole Normale Supérieure). Helpful discussions with Burkhard Rost, Ann McDermott, Wayne Hendrickson (Columbia University) and Daniel Raleigh (Stony Brook) are gratefully acknowledged.

Software written in the course of this research is available upon request. The prediction program discussed in Part II can also be used through its web interface accessible from the lab web site.

Preface

This dissertation discusses two of the projects I worked on as a graduate student in Arthur Palmer's lab at Columbia. Both of the projects deal with protein dynamics. However, the first project, described in Part I, deals with the chemical exchange model of dynamical processes.

On the other hand, the second project discusses dynamical processes that can be thought of as fluctuations near the average or equilibrium state.

The first project is involved in deriving analytical expressions and qualitative results pertaining the NMR phenomena it discusses, while the second project takes a more "black box" approach with regard to NMR: it is assumed that the order parameter S^2 accurately describes the local flexibility of the protein backbone, and machine learning is used in an attempt to predict these characteristics from the protein structure alone.

The results described in the first part of the dissertation were published in [1] and [2], and the n-site generalizations are being submitted by Arthur Palmer and me to the Journal of Magnetic Resonance. The material of these papers was reorganized here for consistency in notation and to remove redundancies.

Part II constitutes the bulk of the manuscript we are preparing for submission to peer review.

Introduction

Proteins undergo large conformational changes during their transition from one functional form to another. Additionally, evidence exists that conformational dynamics governs the *rate* of biomolecular recognition, catalysis and allosteric regulation [3], [4].

The time scales of protein dynamics span a continuous spectrum from picoseconds for small atomic perturbations, to nanoseconds for larger loop motions, to microseconds and more for large conformational changes.

Figure 1 schematically illustrates a conformational energy landscape that includes two interconverting conformational states.

Ideally, we would like to extract the information about the individual states, such as the Larmor frequencies [5] of the nuclei, as well as the transition rates and the equilibrium populations.

The faster, picosecond to nanosecond time-scale dynamics can be thought of as the motion within the individual potential energy "wells". This type of dynamics is also interesting due to the fact that the widths of the "wells" are related to the amount of disorder, *i.e.* the entropy of each conformational state. Therefore, the widths are relevant to the thermodynamic stability of the conformational states. NMR allows us to measure a related quantity that describes the amplitude of the rotational fluctuations of the individual segments of the protein backbone and side-chains [6, 7]

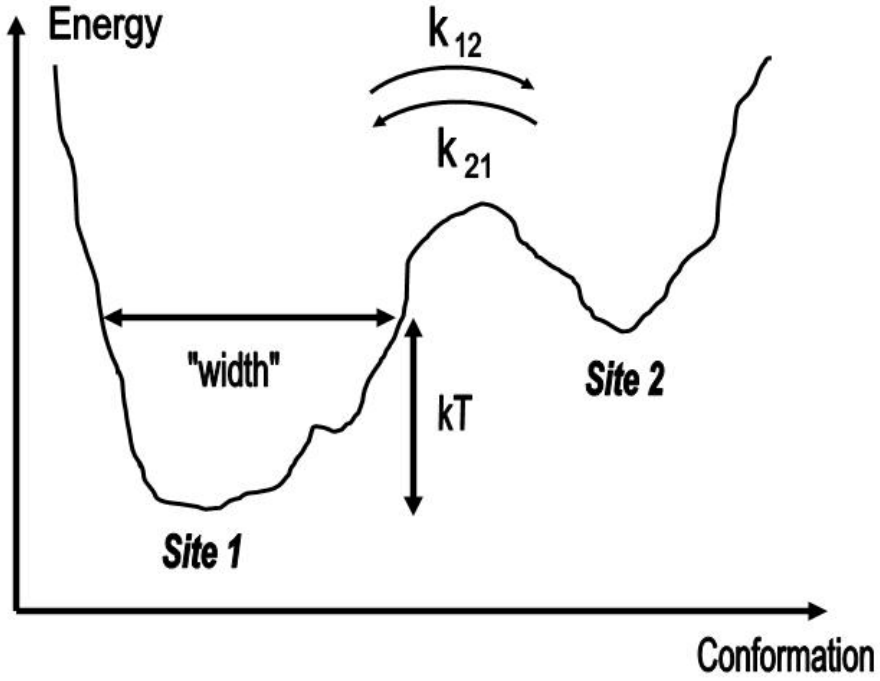

Figure 1: Illustration of the various types of protein conformational dynamics

Part I

Theoretical Study of $R_{1\rho}$ Relaxation and Free Precession in the Presence of Chemical Exchange

1 Introduction

1.1 Chemical Exchange

Chemical exchange is a collective term for dynamical processes that can be modelled as conversions among a finite set of discrete states, where the conversions happen very quickly compared to the life-times of the relatively stable states.

In general, we are interested in a chemical reaction or conformational transition that exchanges a nuclear spin between n sites A_i with distinct

magnetic environments,

$$\begin{array}{ccccccc} & k_{12} & & k_{13} & & k_{ij} & & k_{(n-1)n} & \\ A_1 \rightleftharpoons A_2 & , & A_1 \rightleftharpoons A_3 & , \ldots , & A_i \rightleftharpoons A_j & , \ldots , & A_{n-1} \rightleftharpoons A_n & , \\ & k_{21} & & k_{31} & & k_{ji} & & k_{n(n-1)} & \end{array} \tag{1}$$

in which k_{ij} is the reaction rate constant for the transition from ith to jth site. The chemical kinetics of such a system are described by the equation:

$$\frac{\mathrm{d}}{\mathrm{d}t}\vec{c} = \mathbf{K}\vec{c}, \tag{2}$$

in which the kinetics matrix is given by:

$$\mathbf{K} = \begin{pmatrix} -s_1 & k_{21} & \ldots & k_{n1} \\ k_{12} & -s_2 & \ldots & k_{n2} \\ \vdots & \vdots & \ddots & \vdots \\ k_{1n} & k_{2n} & \ldots & -s_n \end{pmatrix}, \tag{3}$$

$\mathbf{K}_{ij} = k_{ji}$ for $i \neq j$,

$$\mathbf{K}_{ii} = -s_i = - \sum_{\substack{j=1 \\ j \neq i}}^{n} k_{ij}, \tag{4}$$

and the elements of $\vec{c}$ are the site populations of the reacting species. The equilibrium site populations are defined by $\mathbf{K}\vec{c} = 0$.

Although the reactions are depicted in Eq. 1 as first-order, higher-

order ligand-binding or oligomerization reactions can be treated by defining pseudo-first-order rate constants [8]. The kinetic processes are studied by NMR spectroscopy while the system remains in chemical equilibrium.

1.2 $R_{1\rho}$ relaxation in the absence of chemical exchange

The $R_{1\rho}$ experiment consists, essentially, of irradiating the sample, already placed in a strong constant magnetic field, with a radiofrequency (rf) field of constant amplitude and frequency, and observing the time evolution of the nuclear spin magnetization.

The time evolution typically follows a monoexponential decay pattern. The rate constant of the decay, $R_{1\rho}$, is what the name of the experiment is derived from.

In the absence of exchange processes, the time evolution of the nuclear spin magnetization of the individual sites is independent of other sites.

The ith site is characterized by the longitudinal and transverse intrinsic relaxation rates, R_{1i} and R_{2i}, respectively, and the resonance (Larmor) frequency, Ω_i.

If the frequency of the applied rf field is ω_{rf}, and its amplitude, defined by the Rabi frequency, is ω, then the time evolution of the 3-dimensional magnetization of the ith site is given by the Bloch equation [5]:

$$\frac{\mathrm{d}}{\mathrm{d}t}\vec{M}_i = \mathbf{L}_i\vec{M}_i + R_{1i}\vec{M}_{0i}, \tag{5}$$

in which

$$\mathbf{L}_i = \begin{pmatrix} -R_{2i} & -\delta_i & 0 \\ \delta_i & -R_{2i} & -\omega \\ 0 & \omega & -R_{1i} \end{pmatrix}, \tag{6}$$

the resonance offset for the ith site in the rotating frame is defined as

$$\delta_i = \Omega_i - \omega_{rf}, \tag{7}$$

$\vec{M}_i = (M_{xi}, M_{yi}, M_{zi})^{\mathrm{T}}$ is the 3-dimensional Cartesian magnetization vector; $\vec{M}_{0i} = (0, 0, M_{0i})^{\mathrm{T}}$ is the time-independent thermal equilibrium magnetization in the absence of the rf field.

1.3 $R_{1\rho}$ relaxation in the presence of chemical exchange

The state of the n-site system, presented in Eq. 1, is described by a $3n$-dimensional magentization vector

$$\vec{M} = \begin{pmatrix} \vec{M}_1 \\ \vec{M}_2 \\ \vdots \\ \vec{M}_n \end{pmatrix} \tag{8}$$

Its time evolution is a superposition of the precession-relaxation of Eq. 5 and the exchange processes of Eq. 2 and is given by the Bloch-McConnell

equation [9]:

$$\frac{\mathrm{d}}{\mathrm{d}t}\vec{M} = \mathbf{D}\vec{M} + \vec{B}, \tag{9}$$

where

$$\mathbf{D} = \mathbf{L} + \mathbf{K} \otimes \mathbf{1}_s, \tag{10}$$

$$\mathbf{L} = \oplus_{i=1}^{n}\mathbf{L}_i = \begin{pmatrix} \mathbf{L}_1 & & & \\ & \mathbf{L}_2 & & \\ & & \ddots & \\ & & & \mathbf{L}_n \end{pmatrix} \tag{11}$$

$$\vec{B} = \begin{pmatrix} R_{11}\vec{M}_{01} \\ R_{12}\vec{M}_{02} \\ \vdots \\ R_{1n}\vec{M}_{0n} \end{pmatrix}, \tag{12}$$

$\mathbf{1_s}$ is the identity matrix in the spin space, *i.e.* the 3x3 identity matrix, and $\otimes$ and $\oplus$ denote the direct product and sum, respectively.

1.4 Fast and slow exchange

The exchange rates are referred to as slow, intermediate, or fast on the chemical shift time scale, if they are much smaller than, comparable to, or much greater than the differences among the Larmor frequencies.

The Larmor frequencies are proportional to the value of the static magnetic field of the NMR spectrometer; therefore, the time scale of the exchange

process can depend on the NMR spectrometer utilized.

1.5 Previous results

In experimental studies, the dependence of $R_{1\rho}$ on experimental conditions, such as the amplitude and the frequency of the rf field, is used to determine the rate constants, site populations, and Larmor frequencies for nuclear spins affected by the kinetic process.

The most common theoretical expression for $R_{1\rho}$, previously used, requires that exchange kinetics are fast on the chemical shift time scale, *i.e.* the chemical exchange rate constant is much greater than the difference between the Larmor frequencies of the exchanging nuclear spins [10]. Such exchange regime prevents the experimental determination of the individual Larmor frequencies and the site populations independently. An expression also has been reported that is applicable to all kinetic regimes provided that one of the sites is much more populated than others, the frequency of the applied rf field coincides with the population average Larmor frequency, and the longitudinal relaxation rate R_1 equals the transverse relaxation rate R_2 [11]. The restriction of the applied rf field frequency is unfortunate, since, as will be shown below, varying it is a powerful utility.

2 Eigenvalue Problem. RF Field Inhomogeneity.

In general, Eq. 9 is a first-order linear differential equation with constant coefficients. Its solution has the form

$$\vec{M}(t) = \sum_{i=1}^{3n} e^{\lambda_i t}\vec{l_n} + \vec{a}, \tag{13}$$

where λ_i is the ith eigenvalue of the matrix $\mathbf{D}$ in Eq. 10, $\vec{l_i}$ is proportional to the corresponding eigenvector, and $\vec{a}$ is the stationary solution.

For realistic experimental conditions, numerical simulations establish that the matrix $\mathbf{D}$ has n real eigenvalues and n pairs of complex ones with relatively large imaginary parts. In practice, ω varies at different points within the macroscopic NMR sample due to instrumental imperfections. The ω inhomogeneity introduces variability in the eigenvalues and in the orientation of the eigenbasis. While the latter effect is insignificant, eigenvalue inhomogeneity results in rapid, on the time scale of the variation of ω due to the inhomogeneity or faster, averaging of the oscillatory (*i.e.* corresponding to nonreal eigenvalues) components to zero. In many cases of interest, one real eigenvalue is significantly geater than the other $n-1$ ones. On experimentally accessible time scales, the largest (least negative) real eigenvalue dominates the evolution of the magnetization components and the relaxation decay is essentially monoexponential. Thus, the problem of finding the relaxation

rate $R_{1\rho}$ reduces to finding the largest real eigenvalue λ of the matrix $\mathbf{D}$ from Eq. 10:

$$R_{1\rho} = -\lambda \tag{14}$$

Since we are only interested in the eigenvalue of matrix $\mathbf{D}$, we shall ignore the free term in Eq. 9 henceforth.

3 Two sites

3.1 General case

In this section, we consider the simplest and most widely used model of chemical exchange that involves only two sites:

$$A_1 \underset{k_{21}}{\overset{k_{12}}{\rightleftharpoons}} A_2, \tag{15}$$

in which k_{12} is the rate constant for the forward reaction and k_{21} is the rate constant for the reverse reaction.

For two sites, the Bloch-McConnell evolution equation Eq. 9 becomes

$$\frac{\mathrm{d}}{\mathrm{d}t}\begin{pmatrix} \vec{M}_1 \\ \vec{M}_2 \end{pmatrix} = \begin{pmatrix} \mathbf{L}_1 - k_{12} & k_{21} \\ k_{12} & \mathbf{L}_2 - k_{21} \end{pmatrix}\begin{pmatrix} \vec{M}_1 \\ \vec{M}_2 \end{pmatrix}. \tag{16}$$

The matrix in Eq. 16 has a 6x6 dimensionality, and its characteristic

polynomial is of sixth order. The roots of a sixth-order polynomial, in general, can not be found analytically. We are interested in finding a reasonable analytical *approximation* of the largests real eigenvalue.

One approach to finding the eigenvalue closest to zero is to linearize the characteristic polynomial of the matrix [1]. Here, we shall use this approach in combination with what amounts to the steady-state approximation.

In order to characterise the evolution of the average magnetisation, new variables are defined as $\langle\vec{M}\rangle = \vec{M}_1 + \vec{M}_2$ and $\vec{M}_{diff} = p_2\vec{M}_1 - p_1\vec{M}_2$, where p_1 and p_2 are the fractional populations.

In the new variables, the Bloch-McConnell equations are transformed to:

$$\frac{d}{dt}\begin{pmatrix} \langle\vec{M}\rangle \\ \vec{M}_{diff} \end{pmatrix} = \begin{pmatrix} \bar{\mathbf{L}} & -\boldsymbol{\Delta} \\ -p_1p_2\boldsymbol{\Delta} & \mathbf{C} - k \end{pmatrix}\begin{pmatrix} \langle\vec{M}\rangle \\ \vec{M}_{diff} \end{pmatrix}, \tag{17}$$

where

$$\bar{\mathbf{L}} = p_1\mathbf{L}_1 + p_2\mathbf{L}_2, \tag{18}$$

$$\mathbf{C} = p_2\mathbf{L}_1 + p_1\mathbf{L}_2, \tag{19}$$

$$\Delta = \mathbf{L}_2 - \mathbf{L}_1, \tag{20}$$

$$k = k_{12} + k_{21}. \tag{21}$$

The eigenvalue problem for equation (17) is

$$\begin{vmatrix} \bar{\mathbf{L}} - \lambda & -\mathbf{\Delta} \\ -p_1 p_2 \mathbf{\Delta} & \mathbf{C} - k - \lambda \end{vmatrix} = 0. \tag{22}$$

in which $|\ldots|$ denotes the determinant. The determinant of a product is the product of the determinants; therefore, the matrix in Eq. (22) can be multiplied from the left by the following non-degenerate matrix having a determinant of unity:

$$\begin{pmatrix} 1 & \Delta(\mathbf{C} - k - \lambda)^{-1} \\ 0 & 1 \end{pmatrix}. \tag{23}$$

Equation 22 becomes:

$$\begin{vmatrix} \bar{\mathbf{L}} - p_a p_b \Delta(\mathbf{C} - k - \lambda)^{-1} - \lambda & 0 \\ -p_a p_b \mathbf{\Delta} & \mathbf{C} - k - \lambda \end{vmatrix} = 0, \tag{24}$$

which is equivalent to

$$\left|\bar{\mathbf{L}} + p_1 p_2 \Delta(\lambda + k - \mathbf{C})^{-1}\Delta - \lambda\right| = 0. \tag{25}$$

If $\lambda + k - \mathbf{C} \approx k - \mathbf{C}$, then Eq. (25) can be approximated by equation

$$\left|\bar{\mathbf{L}} + p_1 p_2 \Delta(k - \mathbf{C})^{-1}\Delta - \lambda\right| = 0. \tag{26}$$

This assumption is equivalent to the well-known steady-state approximation for solving systems of differential equations.

Equation 26 is of third order in λ. We simplify it further by linearizing it with respect to λ and $r = R_2 - R_1$, *i.e.* keeping terms that are constant or linear, but not bilinear, quadratic or higher-order. We also assume that the intrinsic relaxation rates do not differ between the sites, *i.e.* $R_{11} = R_{12} = R_1$ and $R_{21} = R_{22} = R_2$.

After some tedious simplifications of the resulting linear equation, we can write down the expression for $R_{1\rho} = -\lambda$:

$$R_{1\rho} = R_1 \cos^2\theta + R_2 \sin^2\theta + \frac{\sin^2\theta p_1 p_2 \delta^2 k}{\omega_{e1}^2\omega_{e2}^2/\omega_e^2 + k^2 - 2\sin^2\theta p_1 p_2 \delta^2}, \tag{27}$$

where

$$\bar{\Omega} = p_1\Omega_1 + p_2\Omega_2, \tag{28}$$

$$\Delta\Omega = \bar{\Omega} - \omega_{rf}, \tag{29}$$

$$\delta = \delta_2 - \delta_1 = \Omega_2 - \Omega_1, \tag{30}$$

$$\omega_{e1}^2 = \delta_1^2 + \omega^2, \tag{31}$$

$$\omega_{e2}^2 = \delta_2^2 + \omega^2, \tag{32}$$

$$\omega_e^2 = \Delta\Omega^2 + \omega^2, \tag{33}$$

$$\theta = \arctan(\omega/\Delta\Omega). \tag{34}$$

In the fast-exchange limit, $\omega_{e1}^2\omega_{e2}^2/\omega_e^2 + k^2 - 2\sin^2\theta p_1 p_2 \delta^2 \approx \omega_e^2 + k^2$. Therefore, (27) agrees with the previously derived expression for the relaxation rate constant in the fast-exchange limit [10]:

$$R_{1\rho} = R_1 \cos^2\theta + R_2 \sin^2\theta + \frac{\sin^2\theta p_1 p_2 \delta^2 k}{\omega_e^2 + k^2}. \tag{35}$$

Equation 27 generalizes Eq. 35 and is one of the main results of this section. In the fast-exchange limit, $R_{1\rho}$ does not depend on δ, p_1 and p_2 separately, but only on their combination $p_1 p_2 \delta^2$. Therefore δ, p_1 and p_2 cannot be determined independently of each other. In contrast, outside of the fast-exchange limit, independent determination of δ, p_1 and p_2 is possible due to the dependence of the denominator in Eq. 27 on these parameters through ω_{e1} and ω_{e2}.

The linearized expression given by Eq. 27, the fast-limit expression given by Eq. 35, and the exact numerical solution to are compared in Fig. 2. For the indicated conditions, the linearized result agrees very well with the exact result for all values of k; in contrast, the fast-limit expression agrees well with the exact result when $k/\delta > 4$, but fails for exchange processes that are slower. Numerical simulations for a wider range of conditions indicate that the linearized approximation is accurate except for cases in which site populations are nearly equal and exchange is not in the fast limit. Under these conditions, the assumption that the relaxation decay is dominated by a single damping constant is violated.

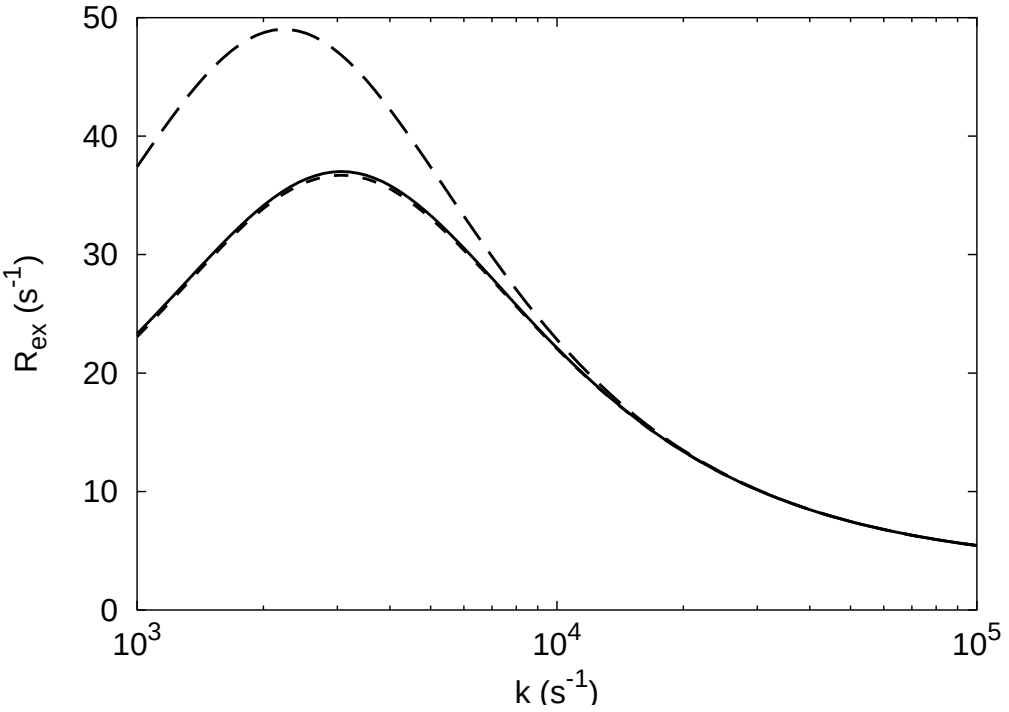

Figure 2: Exchange rate dependence of $R_{1\rho}$. Results are calculated for (—) exact numerical solution, $(\cdots)$ Eq. 27, and (- - -) Eq. 35. Calculations used $\omega = 1000s^{-1}$, $\Delta\Omega = 2000s^{-1}$, $p_2/p_1 = 0.3$, $\delta = 2400s^{-1}$, $R_1 = 1.5s^{-1}$, and $R_2 = 11s^{-1}$.

3.2 Asymmetric populations

In many systems of practical interest, the free energy difference between sites is greater than $k_B T$; consequently, the site populations are unequal because even small differences in energy translate into large population differences through the Boltzman equation [8, 12]. Eq. 27 can be simplified further if one of the sites is much more populated than the other. In the asymmetric-populations limit, $p_1 \gg p_2$; consequently, $\delta_1 \approx \Delta\Omega$ and $\omega_e \approx \omega_{e1}$. Using these relations to simplify Eq. 27, the relaxation rate constant in the asymmetric-populations limit becomes:

$$R_{1\rho} = R_1 \cos^2\theta + R_2 \sin^2\theta + \frac{\sin^2\theta p_1 p_2 \delta^2 k}{\omega_{e2}^2 + k^2}. \tag{36}$$

Eq. 36 generalizes the expression previously reported for the special conditions $R_1 = R_2$ and $\omega_{rf} = \bar{\Omega}$ [11]. This result allows both ω and ω_{rf} to be varied experimentally.

3.3 Experimental data analysis using R_{ex}

From Eq. 27, the relaxation rate constant in the limit $\omega \to \infty$ or $\Delta\Omega \to \infty$ is given by:

$$R_{eff} = R_1 \cos^2\theta + R_2 \sin^2\theta. \tag{37}$$

The excess relaxation rate constant is defined as [13]:

$$R_{ex} \equiv \frac{R_{1\rho} - R_{eff}}{\sin^2 \theta}. \tag{38}$$

Values of R_1 and R_2 can be determined independently from $R_{1\rho}$ [8], which allows R_{ex} to be defined experimentally. From Eqs. (27, 37, 38), the linearized expression for R_{ex} is given by:

$$R_{ex} = \frac{p_1 p_2 \delta^2 k}{\omega_{e1}^2 \omega_{e2}^2 / \omega_e^2 + k^2 - 2 \sin^2 \theta p_1 p_2 \delta^2}. \tag{39}$$

Similarly, from Eqs. [7, 32, 27, 37, 38], the asymmetric-populations limit expression for R_{ex} is:

$$R_{ex} = \frac{p_1 p_2 \delta^2 k}{(\Omega_2 - \omega_{rf})^2 + \omega^2 + k^2}. \tag{40}$$

Finally, from Eqs. [29, 33, 35, 37, 38], the fast-limit expression for R_{ex} is:

$$R_{ex} = \frac{p_1 p_2 \delta^2 k}{(\bar{\Omega} - \omega_{rf})^2 + \omega^2 + k^2}. \tag{41}$$

The asymmetric-populations limit expression given by Eq. 40, the fast-limit expression given by Eq. 41, and the exact numerical solution to the eigenvalue problem are compared in Fig. 3. For the indicated conditions, in which $k/\delta = 0.6$, results calculated using Eq. 40 agree very well with the exact numerical results; in contrast, the fast-limit expression yields dramat-

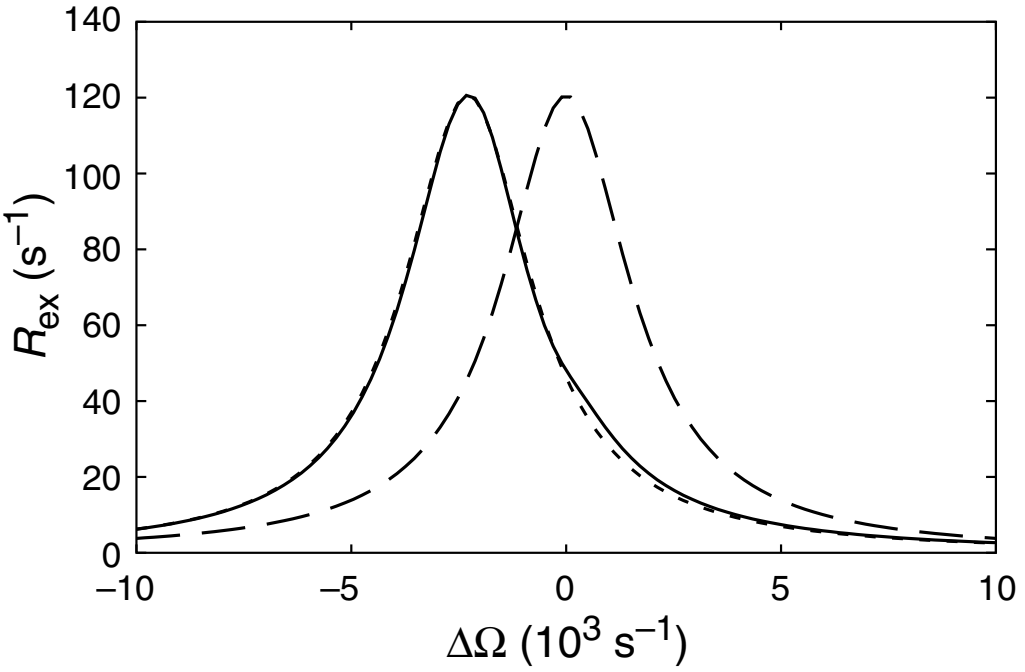

Figure 3: Offset dependence of R_{ex}. Results are calculated for (—) R_{ex} obtained from Eq. 38 using the exact numerical solution, $(\cdots)$ Eq. 40, and (- - -) Eq. 41. Calculations used $\omega = 1000s^{-1}$, $k = 1500s^{-1}$, $p_2/p_1 = 0.05$, $\delta = 2400s^{-1}$, $R_1 = 1.5s^{-1}$, and $R_2 = 11s^{-1}$.

ically different predictions.

As indicated by Eq. 40 and Fig. 3, the maximum value of R_{ex} occurs when the rf frequency is resonant with the Larmor frequency of the minor site B. Thus, in the asymmetric-populations limit, varying the resonance offset at a single static magnetic field strength provides an experimental approach to determining Ω_2 even if p_b is too low to permit direct observation of the corresponding spectral line [12].

4 Multiple sites

Some of the results of the previous chapter can be generalized to the case of $n > 2$ sites:

$$A_1 \underset{k_{21}}{\overset{k_{12}}{\rightleftharpoons}} A_2 \ , \ A_1 \underset{k_{31}}{\overset{k_{13}}{\rightleftharpoons}} A_3 \ , \ldots , \ A_i \underset{k_{ji}}{\overset{k_{ij}}{\rightleftharpoons}} A_j \ , \ldots , \ A_{n-1} \underset{k_{n(n-1)}}{\overset{k_{(n-1)n}}{\rightleftharpoons}} A_n \ . \tag{42}$$

4.1 Asymmetric populations

4.1.1 General case

We consider the case for which the population of the first site is much greater than the populations of others: $p_1 \gg p_2, \ldots, p_n$. Through the detailed balance relationship, this assumption implies that the first column of the kinetics matrix (Eq. 3) $\mathbf{K}$ is much smaller than the rest of the matrix, specifically its first row. By $\mathbf{K}'$, we shall denote the matrix obtained from $\mathbf{K}$ by formally setting its first column to zero. Additionally, R_{1i} and R_{2i} are assumed to be much smaller than other non-trivial components of $\mathbf{L}_i$. We also introduce an approximation of $\mathbf{L}_i$

$$\mathbf{L}'_i = \begin{pmatrix} 0 & -\delta_i & 0 \\ \delta_i & 0 & -\omega \\ 0 & \omega & 0 \end{pmatrix} . \tag{43}$$

Therefore, we can compute the the largest real eigenvalue λ of the matrix $\mathbf{D} = \mathbf{L} + \mathbf{K} \otimes \mathbf{1}_s$ as a perturbed value of the largest real eigenvalue λ' of the

matrix $\mathbf{D}' = \mathbf{L}' + \mathbf{K}' \otimes \mathbf{1}_s$, where $\mathbf{L}' = \oplus_{i=1}^{n} \mathbf{L}_i'$. Examination of $\mathbf{D}'$, shows that the eigenvalue λ' is zero, and the corresponding right eigenvector is

$$\vec{x} = \begin{pmatrix} \vec{v} \\ \vec{0} \\ \vdots \\ \vec{0} \end{pmatrix}, \tag{44}$$

in which $\vec{v}$ is both the left and right eigenvector of $\mathbf{L}_1'$ corresponding to its zero eigenvalue:

$$\vec{v} = \frac{1}{\omega_{e1}} \begin{pmatrix} \omega \\ 0 \\ \delta_1 \end{pmatrix}, \tag{45}$$

and:

$$\omega_{ei} = \sqrt{\delta_i^2 + \omega^2}. \tag{46}$$

The first 3 elements of the corresponding left eigenvector $\vec{y}$ of $\mathbf{D}'$ are also $\vec{v}$. Therefore, the eigenvector can be looked for in the form

$$\vec{y} = \begin{pmatrix} \vec{v} \\ \vec{v} \\ \vdots \\ \vec{v} \end{pmatrix} - \begin{pmatrix} \vec{0} \\ \vec{z}_2 \\ \vdots \\ \vec{z}_n \end{pmatrix} \tag{47}$$

From perturbation theory [14],

$$\lambda = \lambda' + \frac{\vec{y}^{\mathrm{T}}(\mathbf{D} - \mathbf{D}')\vec{x}}{\vec{y}^{\mathrm{T}}\vec{x}}. \tag{48}$$

Using the facts that $\lambda' = 0$, $\vec{y}^{\mathrm{T}}\vec{x} = 1$, and

$$\vec{y}^{\mathrm{T}}(\mathbf{L} - \mathbf{L}')\vec{x} = \vec{v}^{\mathrm{T}}(\mathbf{L}_1 - \mathbf{L}_1')\vec{v} \tag{49}$$

$$= -\frac{\delta_1^2}{\omega_{e1}^2}R_{11} - \frac{\omega^2}{\omega_{e1}^2}R_{21} \tag{50}$$

yields:

$$\lambda = -\frac{\delta_1^2}{\omega_{e1}^2}R_{11} - \frac{\omega^2}{\omega_{e1}^2}R_{21} + \vec{y}^{\mathrm{T}}((\mathbf{K} - \mathbf{K}') \otimes \mathbf{1}_s)\vec{x} \tag{51}$$

Using Eq. 47 and the fact that only the first column of $\mathbf{K} - \mathbf{K}'$ is non-zero, we obtain the following expression for λ:

$$\lambda = -\frac{\delta_1^2}{\omega_{e1}^2}R_{11} - \frac{\omega^2}{\omega_{e1}^2}R_{21} - \sum_{i=2}^{n} k_{1i}\vec{z}_i^{\mathrm{T}}\vec{v}. \tag{52}$$

The values $\vec{z}_i$ are found by substituting Eq. 47 into the definition of the left eigenvector $\vec{y}^{\mathrm{T}}\mathbf{D}' = \lambda'\vec{y}^{\mathrm{T}} = 0$. Transposing and simplifying the resulting expressions, and noting that $\mathbf{L}_i'^{\mathrm{T}} = -\mathbf{L}_i'$, the following equation for the $\vec{z}_i$

values is obtained:

$$\begin{pmatrix} s_2+\mathbf{L}_2' & -k_{23} & \dots & -k_{2n} \\ -k_{32} & s_3+\mathbf{L}_3' & \dots & -k_{3n} \\ \vdots & \vdots & \ddots & \vdots \\ -k_{n2} & -k_{n3} & \dots & s_n+\mathbf{L}_n' \end{pmatrix} \begin{pmatrix} \vec{z}_2 \\ \vec{z}_3 \\ \vdots \\ \vec{z}_n \end{pmatrix} = \begin{pmatrix} \mathbf{L}_2'\vec{v} \\ \mathbf{L}_3'\vec{v} \\ \vdots \\ \mathbf{L}_n'\vec{v} \end{pmatrix} \tag{53}$$

Equation 53 is linear, so it can be solved *symbolically* (and automatically) for any n to give the result:

$$R_{1\rho} = \cos^2\theta_1 R_{11} + \sin^2\theta_1 R_{21} + \sum_{i=2}^{n} k_{1i}\vec{z}_i^{\mathrm{T}}\vec{v}, \tag{54}$$

where $\sin\theta_1 = \omega/\omega_{e1}$ and $\cos\theta_1 = \delta_1/\omega_{e1}$. Equation 54 is one of the primary results of this section.

For convenience, we also define the effective chemical exchange contribution to relaxation as:

$$R_{ex} = R_{1\rho}/\sin^2\theta_1 - R_{11}/\tan^2\theta_1 - R_{21}. \tag{55}$$

From Eqs. 43 and 45, we note (for use in the following) that:

$$(\mathbf{L}_i'+s_i)^{-1} = \begin{pmatrix} s_i & -\delta_i & 0 \\ \delta_i & s_i & -\omega \\ 0 & \omega & s_i \end{pmatrix}^{-1} = \frac{1}{s_i}\frac{1}{s_i^2+\omega_{ei}^2} \begin{pmatrix} s_i^2+\omega^2 & s_i\delta_i & \delta_i\omega \\ -s_i\delta_i & s_i^2 & s_i\omega \\ \delta_i\omega & -s_i\omega & s_i^2+\delta_i^2 \end{pmatrix} \tag{56}$$

and

$$\mathbf{L}_i'\vec{v} = \frac{\omega\Delta\omega_{i1}}{\omega_{e1}} \begin{pmatrix} 0 \\ 1 \\ 0 \end{pmatrix} \tag{57}$$

in which $\Delta\omega_{ij} = \delta_i - \delta_j$. We also define:

$$\vec{z}_i' = (\mathbf{L}_i' + s_i)^{-1}\mathbf{L}_i'\vec{v} = \frac{\omega}{\omega_{e1}} \frac{\Delta\omega_{i1}}{s_i^2 + \omega_{ei}^2} \begin{pmatrix} \delta_i \\ s_i \\ -\omega \end{pmatrix} \tag{58}$$

The following sections consider some special cases of practical interest.

4.1.2 No minor exchange

We refer to the set of all of the exchange reactions that do not involve the dominant site (site 1) as minor exchange. From Eq. 53, in the absence of the minor exchange, $\vec{z}_i = \vec{z}_i'$. Using this result with the understanding that $s_i = k_{i1}$, we obtain:

$$R_{1\rho} = \cos^2\theta_1 R_{11} + \sin^2\theta_1 R_{21} + \sin^2\theta_1 \sum_{i=2}^{n} \frac{k_{1i}\Delta\omega_{i1}^2}{k_{i1}^2 + \omega_{ei}^2} \tag{59}$$

This result generalizes the 2-site expression in Eq. 54. Figure 4 illustrates this expression for a 4-site exchange process. The important qualitative result is that $n-1$ local maxima are obtained when $\delta_i = 0$ for $i = 2, \ldots, n$, *i.e.* when the rf is resonant with the minor sites.

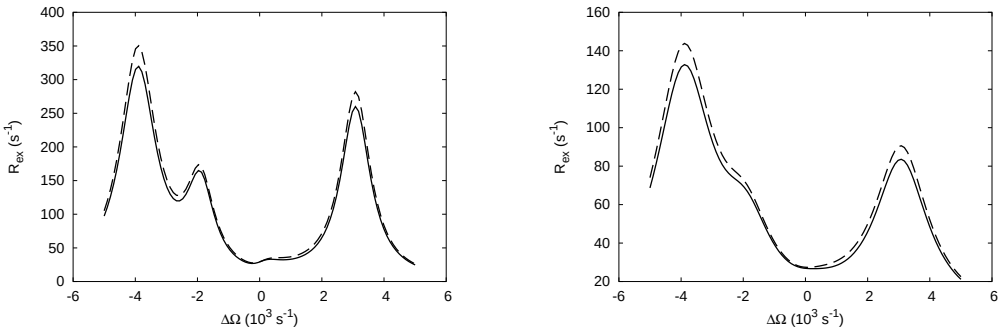

(a) (b)

Figure 4: Offset dependence of R_{ex} for a system with no minor exchange. Solid line represents the exact numerical solution; dashed line shows approximate solution obtained from Eq. 59. Calculations used $p_1 = 0.90$, $p_2 = 0.05$, $p_3 = 0.03$, $p_4 = 0.02$, $\delta_2 - \delta_1 = 2000s^{-1}$, $\delta_3 - \delta_1 = -3000s^{-1}$, $\delta_4 - \delta_1 = 4000s^{-1}$, $k_{12} + k_{21} = 200s^{-1}$, $k_{13} + k_{31} = 200s^{-1}$, $k_{14} + k_{41} = 200s^{-1}$, $R_1 = 1.5s^{-1}$, $R_2 = 11s^{-1}$. $\omega = 500s^{-1}$ (a), $\omega = 1000s^{-1}$ (b). Abscissa indicates the difference between ω_{rf} and the population-average resonance frequency.

4.1.3 Weak minor exchange

We shall call the minor exchange weak, if the rate of conversion from every minor site to the dominant site is much greater than the rates of conversion between minor sites, *i.e.*

$$k_{i1} \gg k_{ij}, \text{ where } i,j = 2,\ldots,n \tag{60}$$

Multiplying Eq. 53 from the left by $\oplus_{i=2}^{n}(\mathbf{L}'_i + s_i)^{-1}$, we obtain:

$$\begin{pmatrix} \mathbf{1}_s & -k_{23}(\mathbf{L}'_2+s_2)^{-1} & \ldots & -k_{2n}(\mathbf{L}'_2+s_2)^{-1} \\ -k_{32}(\mathbf{L}'_3+s_3)^{-1} & \mathbf{1}_s & \ldots & -k_{3n}(\mathbf{L}'_3+s_3)^{-1} \\ \vdots & \vdots & \ddots & \vdots \\ -k_{n2}(\mathbf{L}'_n+s_n)^{-1} & -k_{n3}(\mathbf{L}'_n+s_n)^{-1} & \ldots & \mathbf{1}_s \end{pmatrix} \begin{pmatrix} \vec{z}_2 \\ \vec{z}_3 \\ \vdots \\ \vec{z}_n \end{pmatrix} = \begin{pmatrix} \vec{z}'_2 \\ \vec{z}'_3 \\ \vdots \\ \vec{z}'_n \end{pmatrix}. \tag{61}$$

From Eq. 56, the elements of $(\mathbf{L}'_i + s_i)^{-1}$ obviously do not exceed $1/s_i$ in absolute value, and because $s_i \geq k_{i1}$, the weak minor exchange condition 60 implies that the off-diagonal elements in Eq. 61 are significantly smaller than 1. In the zero-order approximation $\vec{z}_i = \vec{z}'_i$, as in the case of no minor exchange, while the next order of approximation uses the expansion ($\mathbf{1}$ +

$\epsilon\mathbf{X})^{-1} \approx \mathbf{1} - \epsilon\mathbf{X}$:

$$\vec{z}_i \approx \vec{z}'_i + \sum_{\substack{j >= 2 \\ j \neq i}} k_{ij}(\mathbf{L}'_i + s_i)^{-1}\vec{z}'_j \tag{62}$$

Combining this result with Eqs. 54 and 58 yields:

$$R_{1\rho} = \cos^2\theta_1 R_{11} + \sin^2\theta_1 R_{21} + \sin^2\theta_1 \sum_{i=2}^{n} \frac{k_{1i}}{s_i^2 + \omega_{ei}^2}\left[\Delta\omega_{i1}^2 + \frac{1}{s_i}\sum_{\substack{j=2 \\ j\neq i}}^{n} \frac{k_{ij}\Delta\omega_{j1}}{s_j^2+\omega_{ej}^2}((\omega^2 + \delta_1\delta_i)\Delta\omega_{ji} + s_i^2\Delta\omega_{j1} + s_i s_j \Delta\omega_{i1})\right]. \tag{63}$$

Figure 5 illustrates this expression for a 3-site exchange process. The effect of weak minor exchange increases the exchange broadening compared to results obtained in the absence of minor exchange.

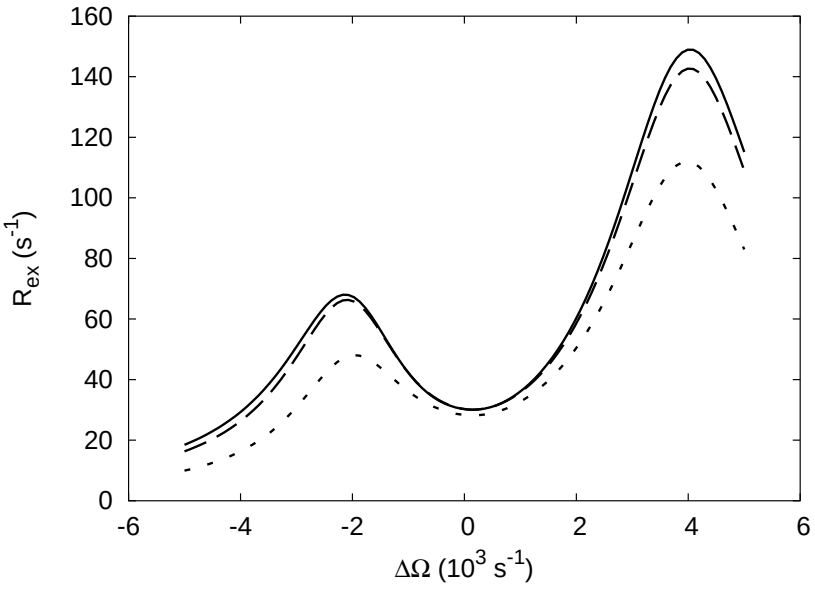

Figure 5: Offset dependence of R_{ex} for a system with weak minor exchange. Solid line represents the exact numerical solution; dashed and dotted lines shows approximate solutions obtained from Eqs. 63 and 59, respectively. Calculations used $\omega = 1000s^{-1}$, $p_1 = 0.95$, $p_2 = 0.03$, $p_3 = 0.02$, $\delta_2 - \delta_1 = 2000s^{-1}$, $\delta_3 - \delta_1 = -4000s^{-1}$, $k_{12} + k_{21} = 500s^{-1}$, $k_{13} + k_{31} = 1000s^{-1}$, $k_{23} + k_{32} = 700s^{-1}$, $R_1 = 1.5s^{-1}$, $R_2 = 11s^{-1}$. Abscissa indicates the difference between ω_{rf} and the population-average resonance frequency.

4.1.4 Population-averaged values

Let us introduce the population-averaged values:

$$\delta = \sum_{i=1}^{n} p_i \delta_i \tag{64}$$

$$\omega_e = \sqrt{\delta^2 + \omega^2} \tag{65}$$

$$\sin\theta = \omega/\omega_e \tag{66}$$

$$\cos\theta = \delta/\omega_e \tag{67}$$

$$R_1 = \sum_{i=1}^{n} p_i R_{1i} \tag{68}$$

$$R_2 = \sum_{i=1}^{n} p_i R_{2i}, \tag{69}$$

The differences resulting from replacing $\sin\theta_1$, $\cos\theta_1$, R_{11}, R_{21} with the respective population-averaged values in Eqs. 54, 55, 59, and 63, are second-order (quadratic or bilinear) in p_i, R_{1j} and R_{2j}, where $i = 2, \ldots, n$, $j = 1, \ldots, n$. Therefore, these differences can be ignored and population-averaged values can be substituted into Eqs. 54, 55, 59, and 63.

4.2 Computational fitting experiments

Equation 59 demonstrates that if minor exchange is absent, the exchange rates are slow, and ω is significantly smaller than any differences among the resonance frequences, then the local maxima of R_{ex} as a function of the offset occur close to where the rf is resonant with the minor species. From

continuity considerations, or from Eq. 63, the same conclusion should apply to systems with weak minor exchange. One result of this section is that such n-site systems can be studied in a similar fashion to the asymmetric 2-site system, as suggested earlier in [1].

Numerical simulations show that even in situations that may be outside of the weak minor exchange limit, where Eqs. 59 and 63 do not strictly apply, and when the system does not necessarily have a dominant site, a plot of R_{ex} as a function of offset frequency often still exhibits $n-1$ Lorentzian-shaped peaks.

Therefore, we sought to examine the feasibility of fitting experimental $R_{1\rho}$ measurements in these cases and to develop an algorithm suitable for this task. To this end, we simulated idealized $R_{1\rho}$ measurements involving a 3-site system in which the rf offsets with respect to the resonance frequency of the first site were taken to be the 30 equidistant points spanning the interval $[-5000, 5000]$, the populations p_1, p_2 and p_3, as well as the intrinsic relaxation rates R_1 and R_2 were assumed known, while the exchange rates and the resonance frequences were to be inferred from the "experimental" $R_{1\rho}$ relaxation rates. The intrinsic relaxation rate constants can be obtained experimentally by a variety of approaches [15]. In practice the population-averaged resonance frequency, instead of the exact knowledge of the resonance frequency of the first site, and any additional known information about the system would be added as contraints.

The system input parameters were chosen to satisfy the following rela-

tionships:

$$\begin{aligned}
\omega &= 1000 \\
0.4 < p_1 &< 0.95 \\
0.02, 0.1(1-p_1) < p_2 &< 0.4(1-p_1) \\
p_3 &= 1 - p_1 - p_2 \\
2000 < \delta_2 - \delta_1 &< 4000 \\
2000 < \delta_1 - \delta_3 &< 4000 \\
100 < k_2, k_{sd}, k_3 &< (\delta_2 - \delta_1)/3, (\delta_1 - \delta_3)/3 \\
R_1 &= 1.5 \\
R_2 &= 11
\end{aligned} \tag{70}$$

where $k_2 = k_{12} + k_{21}$, $k_3 = k_{13} + k_{31}$, $k_{sd} = k_{23} + k_{32}$, all frequencies are in angular units, and exchange rate constants and relaxation rate constant are in units of s^{-1}. The inequalities denote the uniform distributions from which the parameters were selected randomly. Because the site populations are known, only the sum of the forward and reverse exchange rate constants for each pair of sites are required: the individual rate constants can be determined using the detailed balance principle.

Experimentally, only systems with sufficiently low $R_{1\rho}$ values and narrow spectral lines can be studied; therefore, only the systems with the free-precession relaxation rate and the maximum $R_{1\rho}$ values smaller than 100 s^{-1}

were used, which amounted to 35% of the randomly selected systems.

We used the Levenberg-Marquardt non-linear least-squares fitting algorithm [16] as implemented by the MINPACK optimization package [17] to perform parameter fitting, and the LAPACK library [18] for eigenvalue calculations. Naive application of the Levenberg-Marquardt algorithm showed that the minimization problem is fraught with local minima and is subject to divergence (when one of the unknowns becomes very large). Applying the theoretical insights described in earlier sections, specifically the fact that the local minima of R_{ex} occur close to where the rf is resonant with the minor sites, to the initial choice of unknown variables in the optimization procedure significantly improved its convergence properties.

To simulate the experimental error, random values taken from the Gaussian distribution with the standard deviation calculated as a fraction of the maximum $R_{1\rho}$ value for each system were added to the "experimental" $R_{1\rho}$ values.

For each error magnitude, the computational experiment was repeated 1000 times with randomly selected system parameters, as described above. The fitting was considered successful, when the Euclidean distance in the five dimensional parameter space between the "true" parameter values and those returned by the fitting procedure was smaller than 300 s^{-1} The results are summarized in Table 1.

Table 1: Computational fitting experiment results

Error	Success rate	Δ^1 (s^{-1})
1%	99.1%	33
3%	96.7%	99
10%	65.7%	186

[1]Δ is the root mean square deviation from the "true" value

4.3 Free precession evolution

The above formalism is easily adapted to the evolution of transverse magnetization in the absence of radiofrequency fields. The resonance line of the dominant component of the complex magnetization, $M^+(t)$, is described by a resonance frequency and a relaxation rate constant given by:

$$i\Omega - R_2 = i\delta_1 - R_{21} + \lambda \tag{71}$$

in which λ is the eigenvalue of $\mathbf{D} = \mathbf{L} + \mathbf{K}$, $L_i = L_i' = i\Delta\omega_{i1} - \Delta R_{2i}$ with the largest (least negative) real part, and $\Delta R_{2i} = R_{2i} - R_{21}$. Note that for free-precession, $\mathbf{1}_s = 1$. The right eigenvector of $\mathbf{D}'$, corresponding to its zero eigenvalue, is $\vec{x} = (1, 0, \ldots, 0)^{\mathrm{T}}$, and by direct analogy to the above derivation of Eq. 54,

$$i\Omega - R_2 = i\delta_1 - R_{21} - \sum_{i=2}^{n} k_{1i} z_i \tag{72}$$

in which

$$\begin{pmatrix} s_2 - L_2 & -k_{23} & \dots & -k_{2n} \\ -k_{32} & s_3 - L_3 & \dots & -k_{3n} \\ \vdots & \vdots & \ddots & \vdots \\ -k_{n2} & -k_{n3} & \dots & s_n - L_n \end{pmatrix} \begin{pmatrix} z_2 \\ z_3 \\ \vdots \\ z_n \end{pmatrix} = - \begin{pmatrix} L_2 \\ L_3 \\ \vdots \\ L_n \end{pmatrix}. \tag{73}$$

The resonance frequency and relaxation rate constant are obtained from the imaginary and real parts of the right-hand-side of Eq. 72, respectively. Equation 72 is another of the principal results of this paper.

In the absence of minor exchange,

$$\begin{aligned} z_i &= \frac{-i\Delta\omega_i + \Delta R_{2i}}{k_{i1} - i\Delta\omega_i + \Delta R_{2i}} \\ &= \frac{\Delta R_{2i}(k_{i1} + \Delta R_{2i}) + \Delta\omega_i^2 - i\Delta\omega_i k_{i1}}{(k_{i1} + \Delta R_{2i})^2 + \Delta\omega_i^2} \end{aligned} \tag{74}$$

which yields

$$\Omega = \delta_1 + \sum_{i=2}^{n} \frac{k_{1i} k_{i1} \Delta\omega_i}{(k_{i1} + \Delta R_{2i})^2 + \Delta\omega_i^2} \tag{75}$$

$$R_2 = R_{21} + \sum_{i=2}^{n} k_{1i} \frac{\Delta R_{2i}(k_{i1} + \Delta R_{2i}) + \Delta\omega_i^2}{(k_{i1} + \Delta R_{2i})^2 + \Delta\omega_i^2}. \tag{76}$$

These equations extend the results of Skrynnikov and coworkers for 2-site exchange [19]. The n-site Swift-Connick relationships [20] differ from Eqs. 75 and 76 because ΔR_{2i} is replaced by R_{2i}. The present results are more accurate than the Swift-Connick relationships if ΔR_{2i} are small, but R_{2i} are

comparable in magnitude to k_{i1}.

For weak minor exchange,

$$z_i = z_i' + \frac{(s_i + \Delta R_{2i} + i\Delta\omega_i)}{(s_i + \Delta R_{2i})^2 + \Delta\omega_i^2} \sum_{\substack{j=2 \\ j \neq i}}^{n} k_{ij} z_j' \tag{77}$$

in which

$$z_i' = \frac{\Delta R_{2i}(s_i + \Delta R_{2i}) + \Delta\omega_i^2 - i\Delta\omega_i s_i}{(s_i + \Delta R_{2i})^2 + \Delta\omega_i^2} \tag{78}$$

4.3.1 Three sites

For completeness, we provide below some limiting expressions for the exchange contribution to the transverse relaxation rate constant, $R_{ex} = R_2 - R_{21}$, for 3-site chemical exchange. For simplicity, $s_i \gg \Delta R_{2i}$ and $\Delta\omega_i \gg \Delta R_{2i}$ are assumed; thus, $\Delta R_{2i} = 0$ can be utilized in Eqs. 72-78. The general result is derived from Eq. 72. In the absence of minor exchange,

$$R_{ex} = \frac{k_{12}\Delta\omega_2^2}{k_{21}^2 + \Delta\omega_2^2} + \frac{k_{13}\Delta\omega_3^2}{k_{31}^2 + \Delta\omega_3^2} \tag{79}$$

For weak minor exchange,

$$R_{ex} = \frac{k_{12}\Delta\omega_2^2}{s_2^2 + \Delta\omega_2^2} + \frac{k_{13}\Delta\omega_3^2}{s_3^2 + \Delta\omega_3^2} + \frac{(k_{13}k_{32}\Delta\omega_2 + k_{12}k_{23}\Delta\omega_3)(s_3\Delta\omega_2 + s_2\Delta\omega_3)}{(s_2^2 + \Delta\omega_2^2)(s_3^2 + \Delta\omega_3^2)} \tag{80}$$

5 Fast exchange within a subgroup of sites

The following applies equally to $R_{1\rho}$ relaxation and free-precession evolution. Herein, we shall use $\hat{L}_i$ to denote either evolution operator for site i.

Removing the restriction that the population of the first site is much greater than the populations of all others, let us assume that molecules in some of the n sites exchange very rapidly among themselves, in some sense. Without loss of generality, let these sites be numbered m through n.

If the exchange rates involving sites m through n approach infinity, then on physical grounds, these $n-m+1$ sites can be treated as a single effective site. This can be shown by noting that the $(M_m, \ldots, M_n)^{\mathrm{T}}$ vector will have a quasi-steady state value that belongs to the null space of the kinetics matrix corresponding to the "fast" reactions, *i.e.*

$$M_i = \alpha_i M_f \tag{81}$$

where

$$\alpha_i = p_i / \sum_{j=m}^{n} p_j, \tag{82}$$

$$M_f = \sum_{i=m}^{n} M_i. \tag{83}$$

Adding rows m through n of $\mathbf{D}$, and using Eqs. 81 and 83 generates the master equation for the new effective system of m sites. The evolution operators $\hat{L}_i$ for sites 1 through $m-1$ will remain unchanged. The evolution operator

for the effective site $\hat{L}_f$, the new mth site, is the population average:

$$\hat{L}_f = \sum_{i=m}^{n} \alpha_i \hat{L}_i \tag{84}$$

Similarly, the rate constants for the reactions "leaving" the effective site are the population averaged values as well:

$$k_{fj} = \sum_{i=m}^{n} \alpha_i k_{ij}, \text{ where } j < m, \tag{85}$$

while the rate constants for the reactions "entering" the effective site are given by

$$k_{jf} = \sum_{i=m}^{n} k_{ji}, \text{ where } j < m. \tag{86}$$

Establishing the conditions of applicability of these formulas is beyond the scope of this work. The results describe the asymptotic behavior of the system, and are not necessarily valid approximations when the exchange rates involving sites m through n are merely much greater than other exchange rates, the differences between the resonance frequences, offsets, etc. To illustrate this point, consider the case of free-precession involving three sites, where the first site is dominant, $\delta_1 = 0$, $\delta_2 = -\delta_3 = \delta$, $R_{2i} = 0$, and the chemical kinetics are completely symmetric with regard to sites 2 and 3. Then, treating sites 2 and 3 as one effective site predicts $R_{ex} = 0$ if k_{23} is

large. In contrast, the result obtained using Eq. 72 is:

$$R_{ex} = \frac{2k_{12}\delta^2}{k_{21}^2 + 2k_{21}k_{23} + \delta^2}. \tag{87}$$

In this particular case, unless $k_{21}k_{23} \gg \delta^2$, the asymptotic expression is in error by an amount on the order of k_{12}. Figure 6 illustrates the convergence of the free-precession R_2 relaxation rate for a 3-site system to an effective value corresponding to a 2-site system, as the exchange rate between sites 2 and 3 grows, while the site populations and other parameters remain constant.

6 Conclusion

Chemical exchange effects in NMR spectroscopy provide powerful approaches for characterizing kinetic processes, including intramolecular conformational changes, ligand binding, and folding of proteins and other biological macromolecules [8]. Herein, new expressions have been presented that generalize previous theoretical descriptions for the spin relaxation rate constant in the rotating frame, $R_{1\rho}$, for two-site exchange phenomena. The resulting expressions given in Eq. 27, Eq. 54 are accurate provided that the relaxation decay is dominated by a single exponential damping constant. Table 2 summarizes the range of applicability of the previous and new theoretical results for the 2-site case.

The new expressions for $R_{1\rho}$ proved to be very valuable for analyzing

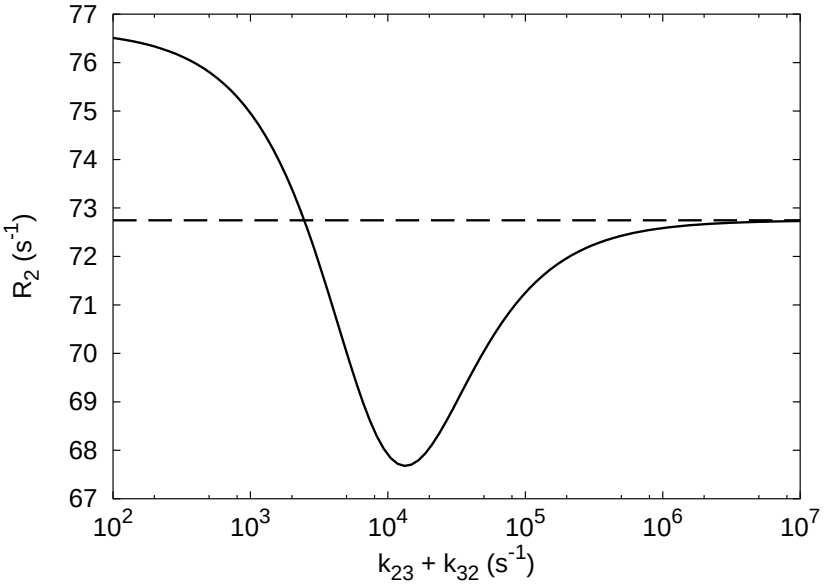

Figure 6: The dependence of free-precession R_2 on the rate of minor exchange. Solid line represents the exact numerical solution; dashed line shows the exact solution for the effective 2-site system obtained using Eqs. 84, 85 and 86. Calculations used $p_1 = 0.80$, $p_2 = 0.13$, $p_3 = 0.07$, $\delta_2 - \delta_1 = 3000s^{-1}$, $\delta_3 - \delta_1 = -3000s^{-1}$, $k_{12} + k_{21} = 300s^{-1}$, $k_{13} + k_{31} = 300s^{-1}$, $R_2 = 11s^{-1}$. Abscissa shows the rate of exchange between sites 2 and 3.

Table 2: Assumptions inherent to existing and new theoretical expressions

Assumptions	Davis [10]	Meiboom [11]	Linearized	Asymmetric
$\omega_{rf} = \bar{\Omega}$	No	Yes	No	No
$R_1 = R_2$	No	Yes	No	No
$k_{12} + k_{21} >> \delta$	Yes	No	No	No
$k_{12} << k_{21}$	No	Yes	No	Yes

experimental data when exchange is not fast and site populations are unequal [21].

In particular, in the asymmetric-populations limit, the $R_{1\rho}$ experiment allows complete characterization of exchange kinetics using data recorded at a single static magnetic field strength. In contrast, to characterize a system outside of the fast-exchange limit, the Carr-Purcell-Meiboom-Gill experiment must be performed at multiple static magnetic field strengths, which requires inconvenient use of different NMR spectrometers subject to systematic variability [22].

For the n-site case, new analytic expressions have been presented that apply to $R_{1\rho}$ and free precession relaxation, when one site population is dominant.

In particular, systems with one dominant site and sufficiently weak exchange among the minor sites will have $R_{ex}(\omega_{rf})$ relaxation dispersion profiles composed of $n-1$ Lorentzians, as a general rule. These results are expected to be generally applicable to the investigation of chemical exchange phenomena in proteins and other biological macromolecules using free-precession and spin-locking techniques.

Part II

Protein Conformational Flexibility Prediction Using Machine Learning

7 Introduction

Dynamical processes in proteins are believed to be closely related to protein function, including ligand-binding, catalysis, and folding, even though this relationship is not yet understood in great detail [23]. Moreover, information about protein conformational flexibility is becoming important in drug design [24]. Thus, considerable importance exists in the related problems of elucidating the microscopic factors that determine protein conformational flexibility and of predicting flexibility from sequence or structural data.

Theoretical assessments of protein flexibility can derive from computational simulations with atomistic and mechanistic detail [25] or from more abstract approaches [26, 27]. Theoretical approaches can be free-standing or aimed at interpretation of experimental measurements of protein flexibility, such as crystallographic B-factors [28].

NMR spin relaxation experiments are widely applied for the study of

the dynamics of macromolecules [6, 7]. NMR spin relaxation data has been collected for various proteins by a number of different research groups, and some of these data have been compiled into publicly accessible data banks [29, 30]. Most commonly, laboratory frame relaxation experiments conducted for ^{15}N [31, 32] or ^{2}H [33, 34] spins have been used to determine the square of the generalized order parameter, S^2, [35] for backbone amide or side chain methyl groups, respectively [6].

A number of authors have used the availability of such NMR data as the basis for further studies of conformational flexibility of proteins. Order parameters derived from NMR have been compared with other experimental and theoretical measures of protein flexibility, including crystallographic B-factors [36], order parameters obtained from fluorescence anisotropy decay measurements [37, 38], and order parameters obtained from molecular dynamics (MD) simulations [39, 40]. Correlations have been uncovered between order parameters and molecular features, such as secondary structural elements and amino acid side chain volumes, [29, 41] and amino acid sequence conservation [42]. Using a database of backbone amide order parameters, Zhang and Brueschweiler empirically devised a simple analytic method for predicting generalized order parameters from static three-dimensional structures [43].

Our goal in the present work is to devise a systematic knowledge-based method for predicting picosecond to nanosecond protein backbone flexibility as described by generalized order parameters obtained from NMR measure-

ments. We are interested in "learning" S^2 as a function of structure from "examples" without necessarily looking in detail into the physics of the process. As "examples", we use backbone ^{15}N order parameters deposited into the Indiana Dynamics Database [29] and the BioMagResBank [30] and the corresponding 3D structures from the Protein Data Bank [44]. We use a particular kind of neural network called a multi-layer perceptron with one hidden layer [45] to optimize the prediction of S^2 given the set of "examples". We anticipate that similar approaches can be applied to predicting slower time scale dynamic properties accessible to NMR experiments [7] and perhaps to computational protein functionality assessments.

8 Methods

Order Parameter. The angular distribution of the orientations of the backbone N-H bond vector on the picosecond to nanosecond time scale is described using the square of the generalized order paramter from the Lipari-Szabo model-free formalism [35]

$$S^2 = (4\pi/5) \sum_{m=-2}^{2} | < Y_{2,m}(\Omega) > |^2, \tag{88}$$

where $Y_{2,m}(\Omega)$ are the second order spherical harmonics, and Ω describes the orientation of the N-H bond vector in the protein-attached coordinate system. In the limiting case of completely isotropic orientation of the bond

vector with respect to the body of the molecule, $S^2 = 0$. Alternatively, $S^2 = 1$, if the orientation is fixed.

Data Banks. Table 3 lists the PDB, IDD and BMRB entries that were used in the present work. As discussed by Goodman *et.al.* [29], some of the systematic differences in S^2 between different data sets are due to the differences in the ways the data were collected and analyzed. Therefore, normalizing S^2 to reduce this artificial variation is beneficial. Goodman *et.al.* divide each S^2 by the average value of S^2 for the protein in which the N-H group resides. We employ a similar linear transformation. However, under the assumption that the true average order parameter of residues in the secondary structure is likely to vary less among different proteins than the order parameter averaged over all residues of the protein, we use the former as the reference point, "normalizing" each database entry so that the average value of S^2 for residues in the *secondary structure* becomes 0.86.

Supervised learning. "Learning from examples" constitutes what is known as the supervised learning or the function approximation problem [45], which is informally stated as follows. Given an unknown function $f(\vec{x})$ and a training set $\{(\vec{x_i}, \vec{y_i})\}_{i=1}^{N}$, for which $\vec{y_i} \approx f(\vec{x_i})$, find an approximation of the unknown function $f(\vec{x})$. This approximation is typically obtained from an adequately general parametrization $F(\vec{x}, \vec{w})$ by optimizing parameters $\vec{w}$. Supervised learning problems can be solved using artifical neural networks. We use a special kind of a neural network called a multi-layer perceptron with one hidden layer [45]. This network architecture corresponds to the parametriza-

Table 3: Dataset composition

Index	PDB entry	Chain ID	S^2 data	Relatives
1	3ci2		IDD 1	
2	1clb		IDD 2	1cdn
3	1cdn		IDD 3	1clb
4	1stg		IDD 4	
5	2bbn	A	IDD 5	
6	1xob		IDD 7	1xoa
7	1xoa		IDD 8	1xob
8	1gpr		IDD 9	
9	1bve	A	IDD 10	
10	1itm		IDD 13	
11	1kun		IDD 25	
12	2fsp		IDD 31	
13	1ngl	A	BMR 4267	
14	1vrf	A	BMR 4096	
15	1d2b	A	BMR 5154	
16	1d3z	A	IDD 11	

tion expression:

$$F = s_2(\mathrm{W}_2 s_1(\mathrm{W}_1\vec{x} + \vec{b_1}) + \vec{b_2}), \tag{89}$$

where weight matrices W_1, W_2 and bias vectors $\vec{b_1}$, $\vec{b_2}$ are the parameters adjusted to fit the training data, and s_1, s_2 are the transfer functions, which we choose to be an elementwise application of the sigmoid function:

$$\mathrm{sigm}(x) = 1/(e^{-x} + 1). \tag{90}$$

The function being approximated is the value of S^2 for the ith amino acid residue; therefore, $f(\vec{x})$ is a scalar. Also, the choice of the sigmoid transfer function in the output layer is particularly convenient, because the order parameters satisfy the inequality $0 \leq S^2 \leq 1$. The universal approximation

theorem [45] implies that this parametrization can approximate any continuous function with values within $[0, 1]$ to any given accuracy, if sufficiently large dimensionalities of W_1, W_2, b_1 and b_2 are allowed.

Features. Instead of using the 3D structure of the protein in some machine-readable form as inputs in the training set, we extracted features of the 3D structure that appear to be statistically related to conformational flexibility, such as local density, the size of amino acid residues, and secondary structure state, and use those features as inputs. Statistical correlations between features and S^2 were measured using the Pearson correlation coefficient, defined by

$$C_{xy} = \frac{x\bar{y} - \bar{x}\bar{y}}{\sigma_x \sigma_y} \tag{91}$$

for two variables x and y. Correlations were considered between S^2 for the N-H bond vector of the ith residue and features for the ith residue and flanking residues in the amino acid sequence. "Position" denotes the position of the residue in the protein chain for which the feature is calculated relative to the position of the residue for which S^2 is measured. Thus, a correlation coefficient reported for feature p and position k indicates that the correlation coefficient was calculated using equation 91 with $x = S_i^2$ and $y = p_{i+k}$ for $i = 1, N$ and N is the number of amino acid residues for which data are available. Ranges of k from -6 to +6 were examined. Correlations between features and S^2 were calculated both by pooling all data for all proteins and by averaging the correlations obtained for individual proteins.

Feature Descriptions. The DSSP (dictionary of secondary structure of

proteins) program [46] classifies the secondary structure state of each residue in the protein as either helix (3_{10}, G; α, H; π, I), or extended sheet (E), β bridge (B), turn (T), bend (S), or "other" (L). The continuum secondary secondary structure assignment DSSPcont [41] extends this method by capturing "uncertainties" of DSSP assignments and assigning an eight-dimensional vector to each residue. The vector can be thought of as the probabilities of the respective DSSP assignments. The sum of all eight elements, therefore, equals 1. Each of the eight DSSPcont probabilities was treated as a feature. In addition, the feature "secondary" was defined as the sum of all DSSPcont values except 'L' and 'S'.

The feature "BB H-bonds energy" is the energy of the backbone-to-backbone H-bonds that involve a given peptide bond, where the energy is calculated in the same manner as by DSSP.

"D_{com}" is the distance between the C_α atom and the center of mass of the non-hydrogen atoms of the protein. "Residue Size" is the number of all non-hydrogen atoms in the residue.

"Tail M" equals 1 if the peptide bond, to which the N-H bond belongs, is M or fewer residues away from N- or C-terminus, and 0 otherwise. For example, in a protein chain with residues numbered from 1 to 100, for residues 3 and 99, "Tail $M = 1$" will be 0, while "Tail $M = 2$" will be 1.

"Loop left" and "Loop right" show the extent of the non-secondary (loop) structure towards the N- and C-terminus, respectively. For a given residue, "Loop right" is one-tenth times the relative position towards the C-terminus

of the first residue with a "secondary" feature (defined above) greater than 0.95 (or 95%). If the residue currently of interest is in secondary structure, "loop right" is 0.0. If such residue is not found (due to a chain break) or is found more than 10 residues away, "loop right" is 1.0. The definition of "loop left" is analogous.

"Bend(-m, 0, m)" is the cosine of the angle formed by vectors $\mathrm{C}_\alpha(i+k-m)\mathrm{C}_\alpha(i+k)$ and $\mathrm{C}_\alpha(i+k+m)\mathrm{C}_\alpha(i+k)$, where $\mathrm{C}_\alpha(n)$, is the C_α atoms of the nth residue.

Distance dependent features, "$g(r_k^X)$", are given by $\sum_j f(r_{X_{i+k},j})$, where $r_{X_{i+k},j}$ is the distance between the jth atom and the atom X in the $(i+k)$th residue. The summation extends over all heavy atoms, including hetero-atoms, but not water molecules. When $X = H$, the reference atom is the amide hydrogen of the $(i+k)th$ residue and heavy atoms in the $(i+k)$th and $(i+k-1)$th residues are not included in the summation. When $X = O$, the reference atom is the carbonyl oxygen of the $(i+k)th$ residue and heavy atoms in the $(i+k)$th and $(i+k+1)$th residues are not included in the summation. When $X = C$, the reference atom is the C^α atom of the residue. The modifier "(BB)" indicates that the the summation involves only the atoms that are part of the backbone (N, C_α, C'). The modifier "(all)" indicates that the summation exends over all residues. The function hard(x) is defined by,

$$\mathrm{hard}(x) = \begin{cases} 1, & \text{if } x \geq 0 \\ 0, & \text{if } x < 0 \end{cases} \tag{92}$$

The notation "1/..." indicates the inverse.

Some of these features are similar to quantities used by other authors. For example, "$\exp(-r_0^H/1\text{Å})$" and "$\exp(-r_{-1}^O/1\text{Å})$" are the components of formula used by Zhang-Brueschweiler to predict S^2 [43]. In addition, "$1/\text{hard}(7\text{Å} - r_0^C)$ (all)" corresponds to the function used by Halle to interpret crystallographic B-factors [28].

Optimization. To find the optimal, in the least-squared sense, values of the parameters W_1, W_2, $\vec{b_1}$, and $\vec{b_2}$, the Levenberg-Marquardt algorithm was used [16, 47]. The learning process was cross-validated by iteratively selecting one of the proteins from the data set, excluding its relatives from the data set, allowing the network to learn S^2 from the remaining set and calculating Pearson correlation between experimental and predicted values of S^2. This step was repeated for all proteins in the dataset. The average correlation was used as a measure of the quality of the prediction process.

9 Results

Correlations between some of the features we examined and the normalized squared order parameters for all proteins in the sample set are summarized in table 4. The average correlations determined by analyzing each protein independently are shown in table 5.

Because of the finite size of the training set, supervised learning can be subject to the problem of overfitting/overtraining. Therefore, the number of adjustible parameters and, consequently, the number of features used by the

Table 4: Dataset-wide correlations between features and S^2 (in percent)

Feature description	Position, k												
	-6	-5	-4	-3	-2	-1	0	+1	+2	+3	+4	+5	+6
$\exp(-r_k^O/1\text{Å})$	4.9	12.8	21.8	28.0	33.7	37.1	32.1	23.9	13.7	4.7	-1.7	-8.5	-9.6
$\exp(-r_k^O/2\text{Å})$	8.4	16.9	27.2	34.2	40.8	44.4	39.1	28.1	17.0	6.8	-1.4	-8.4	-9.3
$\exp(-r_k^O/3\text{Å})$	9.9	18.5	28.6	35.6	42.0	**45.5**	40.6	29.6	18.5	8.2	-0.5	-7.4	-8.4
$\exp(-r_k^O/4\text{Å})$	10.6	19.0	28.8	35.7	41.7	45.1	40.6	30.1	19.2	9.2	0.5	-6.3	-7.5
$\exp(-r_k^O/5\text{Å})$	11.0	19.2	28.5	35.2	41.1	44.3	40.1	30.1	19.6	9.9	1.3	-5.4	-6.7
$\exp(-r_k^O/7\text{Å})$	11.4	18.9	27.4	33.5	38.9	41.9	38.3	29.1	19.4	10.4	2.3	-3.9	-5.5
$\exp(-r_k^O/10\text{Å})$	11.3	17.7	24.8	30.1	34.7	37.3	34.2	26.3	17.8	9.8	2.7	-2.7	-4.4
$1/\exp(-r_k^O/1\text{Å})$	4.9	12.8	21.8	28.0	33.7	37.1	32.1	23.9	13.7	4.7	-1.7	-8.5	-9.6
$1/\exp(-r_k^O/2\text{Å})$	-8.1	-16.6	-25.9	-36.5	-47.7	-54.7	-47.7	-33.6	-21.2	-10.6	-0.1	6.7	8.1
$1/\exp(-r_k^O/3\text{Å})$	-12.1	-20.9	-31.1	-41.9	-52.4	-58.1	-52.3	-38.8	-25.5	-13.1	-1.8	5.5	7.9
$1/\exp(-r_k^O/4\text{Å})$	-14.2	-23.1	-33.6	-44.0	-53.7	-58.7	-53.9	-41.0	-27.3	-14.1	-2.9	4.8	7.5
$1/\exp(-r_k^O/5\text{Å})$	-15.2	-24.2	-34.5	-44.6	-53.4	-58.0	-53.8	-41.2	-27.6	-14.3	-3.2	4.4	7.3
$1/\exp(-r_k^O/7\text{Å})$	-15.5	-24.3	-34.1	-43.3	-51.0	-54.8	-50.7	-38.6	-25.6	-13.0	-2.8	4.3	6.9
$1/\exp(-r_k^O/10\text{Å})$	-13.9	-21.5	-30.0	-37.6	-43.8	-46.7	-42.7	-31.6	-20.4	-9.9	-1.6	4.2	6.2
$\exp(-r_k^H/1\text{Å})$	-4.6	-1.2	3.2	9.8	16.3	26.0	33.6	33.3	31.1	22.3	16.5	10.3	8.2
$\exp(-r_k^H/2\text{Å})$	-1.5	3.9	11.3	20.1	28.4	39.8	**46.5**	43.0	36.9	27.0	17.9	8.8	5.0
$\exp(-r_k^H/3\text{Å})$	0.4	6.5	14.3	23.3	31.6	41.9	47.4	43.1	35.7	26.6	17.0	7.8	3.5
$\exp(-r_k^H/4\text{Å})$	1.5	7.7	15.3	24.1	32.1	41.6	46.4	42.0	34.5	25.9	16.6	7.6	3.2
$\exp(-r_k^H/5\text{Å})$	2.3	8.4	15.7	24.2	31.9	40.7	45.1	40.8	33.4	25.2	16.2	7.7	3.3
$\exp(-r_k^H/7\text{Å})$	3.6	9.2	15.8	23.4	30.5	38.3	42.0	38.0	31.1	23.7	15.4	7.7	3.4
$\exp(-r_k^H/10\text{Å})$	4.8	9.5	15.1	21.4	27.3	33.9	36.8	33.2	27.1	20.7	13.6	7.1	3.2
$1/\exp(-r_k^H/1\text{Å})$	2.1	-2.0	-7.4	-15.5	-22.7	-33.6	-38.5	-40.2	-34.1	-25.6	-16.3	-11.2	-8.5
$1/\exp(-r_k^H/2\text{Å})$	0.1	-6.2	-14.1	-24.5	-34.9	-48.2	-53.8	-51.6	-43.8	-32.1	-20.8	-11.5	-6.7
$1/\exp(-r_k^H/3\text{Å})$	-1.7	-9.0	-17.9	-29.1	-39.9	-53.1	-58.7	-55.3	-46.6	-34.2	-22.2	-11.3	-5.4
$1/\exp(-r_k^H/4\text{Å})$	-2.8	-10.7	-19.8	-30.9	-41.5	-54.0	-59.4	-55.9	-46.9	-34.5	-22.3	-11.1	-4.9
$1/\exp(-r_k^H/5\text{Å})$	-3.5	-11.6	-20.7	-31.5	-41.7	-53.6	-58.7	-55.1	-45.9	-33.7	-21.6	-10.6	-4.4
$1/\exp(-r_k^H/7\text{Å})$	-4.2	-12.0	-20.7	-30.8	-40.0	-50.7	-55.1	-50.9	-41.4	-29.9	-18.8	-9.0	-3.4
$1/\exp(-r_k^H/10\text{Å})$	-4.6	-10.8	-18.1	-26.3	-33.9	-42.7	-46.2	-41.3	-32.5	-22.7	-13.8	-6.3	-1.9
$\text{sigm}(3\text{Å} - r_k^H)$	-3.5	0.2	6.0	13.1	20.5	31.6	39.0	37.7	34.2	24.7	17.4	10.3	7.4
$\text{sigm}(4\text{Å} - r_k^H)$	-2.9	1.3	7.9	15.5	23.3	34.8	41.8	39.7	35.1	25.6	17.5	9.6	6.3
$\text{sigm}(5\text{Å} - r_k^H)$	-2.0	2.8	10.1	18.2	26.2	37.9	44.2	41.0	35.4	25.9	17.2	8.4	4.9
$\text{sigm}(7\text{Å} - r_k^H)$	-0.2	5.8	13.4	22.2	30.2	41.0	46.4	41.5	34.1	25.2	15.7	6.2	2.2
$\text{sigm}(10\text{Å} - r_k^H)$	1.7	7.6	15.3	24.1	31.6	40.7	45.2	39.7	31.9	23.7	14.5	5.5	1.1
$1/\text{sigm}(3\text{Å} - r_k^H)$	1.7	-2.9	-8.9	-17.5	-25.8	-37.5	-42.9	-43.4	-37.1	-27.8	-17.7	-11.4	-8.1
$1/\text{sigm}(4\text{Å} - r_k^H)$	1.4	-3.7	-10.2	-19.3	-28.4	-40.7	-46.5	-45.8	-39.1	-29.2	-18.6	-11.3	-7.5
$1/\text{sigm}(5\text{Å} - r_k^H)$	0.9	-4.8	-12.0	-21.7	-31.5	-44.6	-50.7	-48.5	-41.1	-30.5	-19.5	-10.9	-6.6
$1/\text{sigm}(7\text{Å} - r_k^H)$	-0.5	-7.4	-15.6	-26.3	-36.8	-50.7	-56.9	-52.3	-43.4	-31.9	-20.5	-9.8	-4.3
$1/\text{sigm}(10\text{Å} - r_k^H)$	-2.6	-10.1	-18.8	-29.9	-40.1	-53.2	-59.2	-54.3	-45.0	-33.1	-21.4	-9.6	-3.0
$\text{hard}(3\text{Å} - r_k^H)$	-1.7	-1.7	-2.2	2.9	4.7	11.5	16.4	18.7	18.6	13.1	9.9	8.5	9.6
$\text{hard}(4\text{Å} - r_k^H)$	-5.0	-2.1	1.6	7.0	12.4	21.0	27.9	28.4	27.8	20.1	15.0	9.9	8.0
$\text{hard}(5\text{Å} - r_k^H)$	-2.6	-0.7	5.3	9.8	16.1	24.8	31.2	31.6	28.4	20.3	14.5	9.3	7.4
$\text{hard}(7\text{Å} - r_k^H)$	-2.0	4.1	11.9	20.3	28.4	39.8	44.5	40.0	33.0	23.8	14.7	5.7	2.3
$\text{hard}(10\text{Å} - r_k^H)$	1.7	7.6	14.7	23.1	30.6	39.4	44.3	38.5	31.1	23.3	14.1	5.2	1.0
$\exp(-r_k^N/3\text{Å})(\text{BB})$	2.1	7.6	16.2	25.9	34.9	43.6	48.4	43.4	35.5	25.6	15.7	6.2	0.7
$1/\text{hard}(7\text{Å} - r_k^C)$ (all)	-2.1	-8.9	-18.4	-29.5	-40.5	-52.4	-52.8	-41.3	-29.6	-17.7	-7.3	0.7	4.3
D_{com}	-3.4	-10.3	-19.3	-27.9	-33.7	-38.7	-38.8	-32.6	-25.3	-17.4	-8.8	-1.6	2.1
Tail, $M = 1$	-7.4	-8.7	-10.6	-14.1	-20.5	-21.7	-36.5	-16.3	-9.1	-2.8	2.3	2.8	3.9
Tail, $M = 2$	-7.4	-9.6	-11.9	-15.1	-21.2	-40.1	-42.3	-22.0	-8.3	-0.5	3.6	4.8	5.5
Tail, $M = 3$	-6.5	-9.5	-12.4	-15.8	-36.6	-41.9	-41.8	-26.7	-10.9	1.3	5.2	6.2	8.0
Tail, $M = 4$	-4.7	-8.5	-12.2	-31.2	-38.5	-41.1	**-39.3**	-26.4	-15.9	-2.2	6.5	8.4	9.2
Tail, $M = 5$	-2.9	-6.7	-26.3	-33.5	-38.1	-38.7	-36.5	-25.1	-17.0	-8.2	3.5	9.5	10.5
Tail, $M = 6$	-1.9	-20.0	-27.5	-32.7	-35.8	-35.9	-33.7	-23.6	-17.0	-9.6	-2.7	6.1	10.7
DSSPcont G	-7.2	-9.3	-13.4	-10.2	-4.9	-1.9	-0.1	-2.2	-4.7	-2.6	0.3	3.1	1.2
DSSPcont H	-5.4	0.1	5.7	12.1	16.2	19.1	22.7	21.2	16.9	11.8	6.5	2.6	-1.1
DSSPcont I	-6.4	-14.3	-14.2	-3.4	-0.5	1.0	1.2	0.9	-0.5	-1.7	2.2	3.0	1.4
DSSPcont T	3.3	1.1	-1.5	-6.0	-3.8	0.5	1.4	0.1	2.1	2.3	3.7	7.7	8.9
DSSPcont E	2.7	5.5	7.7	10.7	14.2	16.7	14.9	9.6	5.6	0.6	-2.4	-0.8	-1.4
DSSPcont B	4.2	2.8	2.4	1.8	-0.1	0.9	3.4	-2.9	-0.1	-4.1	-5.7	-4.1	-7.5
DSSPcont S	8.0	2.8	0.8	-8.5	-14.8	-15.6	-20.1	-14.6	-8.4	-4.4	0.9	0.9	2.6
DSSPcont L	-2.1	-4.3	-8.8	-12.7	-21.4	-33.2	**-33.8**	-26.9	-22.4	-12.4	-8.6	-10.0	-4.9
Secondary	-3.2	1.8	7.0	16.1	27.3	37.7	**41.5**	32.0	24.3	13.3	6.6	7.8	2.4
Bend (-1, 0, 1)	1.6	0.9	-0.9	-4.2	-8.6	-15.7	**-16.7**	-14.6	-13.2	-11.1	-9.8	-9.0	-5.1
Bend (-2, 0, 2)	3.3	2.8	1.3	-1.5	-5.1	-8.3	-10.1	-12.2	-12.0	-11.4	-10.8	-10.2	-6.4
loop left	-3.8	-5.8	-9.5	-14.5	-22.6	-28.6	-32.0	-37.6	-35.5	-33.9	-30.3	-30.1	-27.5
loop right	-14.4	-19.0	-25.7	-36.0	-40.4	-37.6	-37.6	-17.4	-5.3	1.1	3.9	3.8	4.3
Residue Size	-6.4	-1.5	-0.2	4.1	6.4	9.0	10.0	7.2	6.4	2.3	-1.2	-4.1	-6.0
BB H-bonds energy	5.1	-2.5	-7.8	-15.3	-22.3	-27.1	-34.1	-31.3	-26.6	-16.0	-10.0	-2.8	0.8

Table 5: Average correlations between features and S^2 (in percent)

Feature description	Position, k												
	-6	-5	-4	-3	-2	-1	0	+1	+2	+3	+4	+5	+6
$\exp(-r_k^O/1\text{Å})$	5.0	13.6	23.0	29.1	34.4	38.8	32.8	21.5	12.2	1.8	-3.7	-11.8	-11.7
$\exp(-r_k^O/2\text{Å})$	8.1	16.9	27.2	33.7	40.5	44.8	38.8	24.1	13.6	1.7	-6.5	-14.6	-14.0
$\exp(-r_k^O/3\text{Å})$	9.2	18.0	28.1	34.7	41.6	**45.8**	40.2	24.9	14.2	2.2	-7.3	-15.2	-14.6
$\exp(-r_k^O/4\text{Å})$	9.5	18.3	28.2	34.9	41.8	45.9	40.7	25.4	14.6	2.7	-7.4	-15.1	-14.7
$\exp(-r_k^O/5\text{Å})$	9.5	18.3	28.1	34.9	41.8	45.9	40.9	25.7	14.9	3.1	-7.2	-14.9	-14.6
$\exp(-r_k^O/7\text{Å})$	9.4	18.2	28.0	34.9	41.7	45.8	41.1	26.1	15.4	3.7	-7.0	-14.4	-14.4
$\exp(-r_k^O/10\text{Å})$	9.3	18.0	27.8	34.8	41.7	45.8	41.3	26.5	15.8	4.2	-6.7	-13.9	-14.2
$1/\exp(-r_k^O/1\text{Å})$	5.0	13.6	23.0	29.1	34.4	38.8	32.8	21.5	12.2	1.8	-3.7	-11.8	-11.7
$1/\exp(-r_k^O/2\text{Å})$	-6.4	-14.0	-23.0	-33.1	-42.3	-51.8	-45.2	-26.1	-16.9	-5.0	4.8	12.2	11.2
$1/\exp(-r_k^O/3\text{Å})$	-8.4	-16.1	-25.9	-36.1	-45.1	-53.9	-48.1	-29.1	-19.2	-6.0	5.0	12.4	12.4
$1/\exp(-r_k^O/4\text{Å})$	-9.2	-17.0	-27.2	-37.2	-45.9	-53.9	-48.7	-30.3	-20.2	-6.7	5.0	12.4	12.9
$1/\exp(-r_k^O/5\text{Å})$	-9.5	-17.4	-27.8	-37.6	-46.1	-53.5	-48.6	-30.7	-20.5	-7.0	5.0	12.4	13.2
$1/\exp(-r_k^O/7\text{Å})$	-9.7	-17.7	-28.3	-37.7	-45.7	-52.4	-47.8	-30.7	-20.5	-7.1	5.0	12.3	13.3
$1/\exp(-r_k^O/10\text{Å})$	-9.6	-17.8	-28.4	-37.4	-45.1	-51.1	-46.6	-30.2	-19.9	-7.0	5.1	12.3	13.4
$\exp(-r_k^H/1\text{Å})$	-4.3	-1.2	2.7	8.1	15.7	26.6	36.0	35.0	33.9	23.0	18.3	9.1	8.7
$\exp(-r_k^H/2\text{Å})$	-3.0	2.5	9.9	17.8	26.2	39.2	**48.3**	43.0	36.9	24.5	15.4	4.0	1.1
$\exp(-r_k^H/3\text{Å})$	-2.0	4.2	12.4	21.0	29.4	41.5	49.4	42.8	35.1	23.0	12.9	1.6	-2.2
$\exp(-r_k^H/4\text{Å})$	-1.6	4.7	13.2	21.9	30.2	41.7	49.0	42.1	33.9	22.3	11.8	0.9	-3.4
$\exp(-r_k^H/5\text{Å})$	-1.4	4.9	13.4	22.2	30.5	41.6	48.6	41.6	33.3	21.9	11.3	0.7	-3.8
$\exp(-r_k^H/7\text{Å})$	-1.4	4.9	13.5	22.4	30.6	41.4	48.1	41.2	32.8	21.6	10.9	0.7	-4.1
$\exp(-r_k^H/10\text{Å})$	-1.4	4.9	13.4	22.4	30.6	41.3	47.7	40.9	32.5	21.5	10.7	0.8	-4.2
$1/\exp(-r_k^H/1\text{Å})$	2.9	0.2	-4.2	-9.8	-17.8	-31.4	-39.3	-39.0	-37.1	-23.8	-16.9	-8.2	-5.9
$1/\exp(-r_k^H/2\text{Å})$	2.5	-2.5	-9.3	-17.6	-27.4	-43.0	-52.5	-47.9	-42.8	-27.2	-16.2	-5.4	-1.2
$1/\exp(-r_k^H/3\text{Å})$	1.8	-3.9	-11.7	-21.6	-31.3	-46.5	-55.7	-49.5	-42.5	-27.0	-15.0	-3.7	1.5
$1/\exp(-r_k^H/4\text{Å})$	1.5	-4.5	-12.7	-23.0	-32.6	-47.1	-55.8	-49.1	-41.4	-26.7	-14.3	-3.1	2.6
$1/\exp(-r_k^H/5\text{Å})$	1.3	-4.8	-13.1	-23.6	-33.1	-47.0	-55.2	-48.3	-40.4	-26.4	-13.9	-2.8	3.1
$1/\exp(-r_k^H/7\text{Å})$	1.2	-5.0	-13.5	-24.0	-33.2	-46.2	-53.8	-46.9	-38.9	-25.8	-13.4	-2.6	3.4
$1/\exp(-r_k^H/10\text{Å})$	1.3	-5.0	-13.6	-23.9	-32.9	-45.2	-52.3	-45.5	-37.3	-24.9	-12.7	-2.3	3.6
$\text{sigm}(3\text{Å} - r_k^H)$	-4.2	-0.5	5.1	11.1	19.2	31.9	41.5	38.9	36.2	24.5	18.2	7.9	6.4
$\text{sigm}(4\text{Å} - r_k^H)$	-4.1	0.3	6.9	13.4	21.6	34.8	44.2	40.4	36.4	24.5	17.2	6.2	4.2
$\text{sigm}(5\text{Å} - r_k^H)$	-3.6	1.7	9.0	16.1	24.3	37.6	46.4	41.2	35.8	23.8	15.4	4.1	1.5
$\text{sigm}(7\text{Å} - r^H)$	-2.2	4.4	12.3	20.5	28.2	40.5	48.1	41.2	33.3	21.8	11.9	0.6	-2.8
$\text{sigm}(10\text{Å} - r_k^H)$	-0.1	5.6	13.8	22.4	29.7	40.2	46.9	39.3	30.8	20.0	9.6	-1.0	-5.3
$1/\text{sigm}(3\text{Å} - r_k^H)$	3.0	-0.4	-5.5	-11.8	-20.6	-35.1	-44.0	-42.0	-39.5	-25.6	-17.1	-7.5	-4.7
$1/\text{sigm}(4\text{Å} - r_k^H)$	3.1	-1.0	-6.8	-13.7	-22.8	-37.9	-47.2	-43.8	-40.6	-26.3	-16.9	-6.6	-3.4
$1/\text{sigm}(5\text{Å} - r_k^H)$	3.1	-1.8	-8.4	-16.2	-25.6	-41.2	-50.7	-45.8	-41.2	-26.4	-16.1	-5.3	-1.7
$1/\text{sigm}(7\text{Å} - r_k^H)$	2.3	-3.8	-11.3	-21.0	-30.1	-45.7	-55.3	-48.1	-40.8	-25.6	-13.9	-2.8	1.9
$1/\text{sigm}(10\text{Å} - r_k^H)$	0.5	-5.2	-13.2	-23.9	-32.4	-46.5	-55.6	-47.9	-39.4	-24.9	-12.7	-1.6	4.3
$\text{hard}(3\text{Å} - r_k^H)$	-0.2	-0.8	-3.3	0.7	4.4	12.6	17.6	20.8	21.5	14.1	12.3	9.3	12.9
$\text{hard}(4\text{Å} - r_k^H)$	-5.2	-2.8	0.6	5.6	13.2	22.6	31.5	31.5	32.3	22.7	19.1	10.5	9.8
$\text{hard}(5\text{Å} - r_k^H)$	-3.7	-1.5	4.6	7.8	15.3	25.5	33.7	32.7	31.4	21.3	16.4	7.3	6.7
$\text{hard}(7\text{Å} - r_k^H)$	-4.6	3.0	11.2	19.1	26.8	39.3	46.3	39.9	32.7	20.7	11.6	0.8	-2.0
$\text{hard}(10\text{Å} - r_k^H)$	0.1	5.8	13.3	21.4	28.5	38.8	45.8	38.2	30.1	19.8	9.5	-1.2	-5.0
$\exp(-r_k^N/3\text{Å})(\text{BB})$	-1.9	4.8	13.8	23.5	33.3	44.7	50.6	43.4	34.1	22.1	11.3	0.5	-5.2
$1/\text{hard}(7\text{Å} - r_k^C)$ (all)	-0.1	-7.6	-16.5	-26.8	-38.1	-53.5	-51.1	-36.7	-25.6	-12.8	-1.5	7.4	10.0
D_{com}	-3.3	-10.3	-19.3	-28.1	-34.6	-42.2	-42.7	-32.2	-22.8	-12.8	-1.4	7.0	10.1
Tail, $M = 1$	-5.7	-6.0	-7.6	-10.6	-17.4	-23.4	-40.8	-12.3	-10.8	-5.3	3.1	1.7	4.6
Tail, $M = 2$	-5.3	-6.5	-8.5	-10.8	-17.3	-41.0	-45.1	-26.1	-9.9	-3.3	2.7	4.3	6.4
Tail, $M = 3$	-4.8	-6.0	-8.3	-11.1	-33.0	-41.3	-42.1	-29.7	-15.4	-1.2	5.1	6.1	9.6
Tail, $M = 4$	-3.0	-5.6	-7.7	-27.2	-34.1	-39.7	**-38.5**	-27.4	-19.4	-6.0	6.7	8.9	11.2
Tail, $M = 5$	-1.2	-3.9	-22.7	-28.6	-33.9	-36.5	-34.8	-25.1	-18.5	-10.4	2.2	10.6	12.6
Tail, $M = 6$	-0.9	-17.3	-23.4	-28.4	-31.3	-33.3	-31.7	-22.5	-17.1	-9.7	-2.6	5.3	12.8
DSSPcont G	-5.1	-9.0	-15.2	-11.6	-5.4	-2.8	-0.7	-2.1	-2.7	-0.4	0.8	6.5	4.6
DSSPcont H	-6.4	-0.4	5.9	13.1	17.9	22.0	26.3	25.3	21.4	16.5	10.7	6.5	2.4
DSSPcont I	-3.4	-6.0	-5.7	-2.5	-0.4	-2.4	0.0	0.3	0.9	0.8	2.0	3.5	2.9
DSSPcont T	2.1	-1.4	-3.1	-9.7	-7.5	-1.5	-1.1	-3.7	-0.3	2.3	4.5	9.3	10.2
DSSPcont E	2.7	5.9	7.3	10.1	12.8	14.9	11.6	4.9	-0.1	-6.9	-12.4	-9.4	-9.3
DSSPcont B	5.5	3.9	3.1	1.4	-0.3	-0.0	3.3	0.4	0.6	-2.8	-1.5	1.9	-5.5
DSSPcont S	8.7	3.3	1.0	-7.5	-14.3	-15.1	-19.5	-14.3	-9.0	-3.4	1.1	0.2	4.2
DSSPcont L	-0.3	-1.3	-6.5	-11.4	-21.5	-36.4	**-37.0**	-27.4	-19.9	-10.7	-1.5	-4.0	1.1
Secondary	-5.4	-0.8	5.0	14.5	26.5	39.2	**42.9**	31.4	22.0	10.5	0.7	3.5	-3.0
Bend (-1, 0, 1)	2.4	1.6	-0.6	-4.5	-10.0	-21.4	**-23.2**	-20.3	-18.0	-16.2	-13.0	-11.0	-7.0
Bend (-2, 0, 2)	2.6	2.1	0.5	-2.6	-7.0	-11.8	-15.5	-18.6	-17.7	-17.1	-14.7	-12.7	-9.0
loop left	-0.9	-1.5	-4.5	-8.0	-14.8	-22.4	-24.6	-24.8	-16.0	-12.1	-9.0	-7.2	-6.7
loop right	-8.6	-8.3	-15.4	-20.9	-24.3	-26.4	-34.8	-14.4	-5.7	-0.8	4.7	3.7	5.2
Residue Size	-5.2	-0.6	0.4	4.7	7.6	10.4	9.4	8.5	8.1	1.8	1.1	-6.2	-8.0
BB H-bonds energy	7.4	-1.4	-7.3	-15.3	-23.1	-28.5	-35.5	-32.8	-26.7	-14.6	-6.7	0.9	3.8

Table 6: Optimized weights and bias parameters

Feature	Parameter	Value
$\exp(-r_{-1}^{O}/3\text{Å})$	$W_1(1)$	-2.56
$\exp(-r_{0}^{H}/2\text{Å})$	$W_1(2)$	-1.94
Secondary, $k = 0$	$W_1(3)$	-0.821
DSSPcont L, $k = 0$	$W_1(4)$	-0.270
Bend(-1,0,1), $k = 0$	$W_1(5)$	0.292
Tail, $M = 4$, $k = 0$	$W_1(6)$	0.730
	$\vec{b_1}$	0.652
	W_2	-4.64
	$\vec{b_2}$	2.01

network, must be limited. After some experimentation, we decided to use just one hidden unit and six features. The cells of tables 4 and 5 corresponding to the features presently incoportated into the model are marked in bold font and underlined.

The optimized values of the model parameters are shown in table 6. The results of cross-validating the optimized parameters for these features are shown in figure 7. Although the predictions themselves are affected by the initial normalization of the S^2, the average correlation used as the measure of the prediction quality is the same, whether we compare the predictions to the normalized S^2 or the original unnormalized data. The average correlation between experimental and predicted values of S^2 during the cross-validation procedure equals 71.4%.

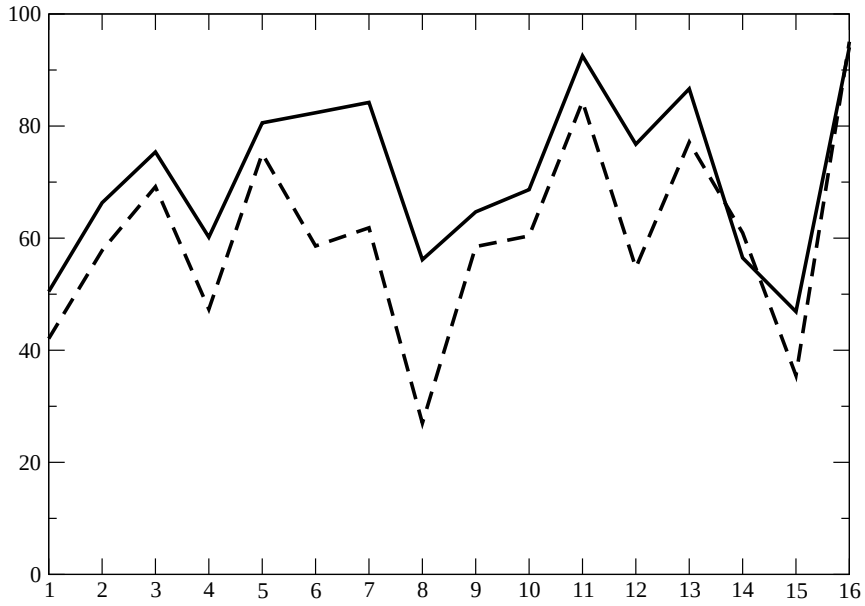

Figure 7: Correlations between predicted and experimental S^2. (- - -) Zhang-Brueschweiler formula; (—) neural network predictions during cross-validation. Abscissa shows the protein index from table 3

Figure 8: The backbones of the first 5 NMR models of the forkhead domain of the adipocyte-transcription factor freac-11 (S12) (PDB code: 1D5V)

10 Sensitivity to Structure

To illustrate the sensitivity of the predictions to the protein structure, Figure 9 shows the S^2 predictions for the first 5 NMR models of the forkhead domain of the adipocyte-transcription factor freac-11 (S12) (PDB code: 1D5V) (Shown in Figure 8).

11 Discussion and Conclusion

Correlations have been examined for features for residues in positions -6 to $+6$ relative to the residue for which S^2 is to be predicted. The correlations shown in tables 4 and 5 are dominated by residues in the -1, 0, and $+1$ positions. Features for residues in positions further away are much less correlated with S^2.

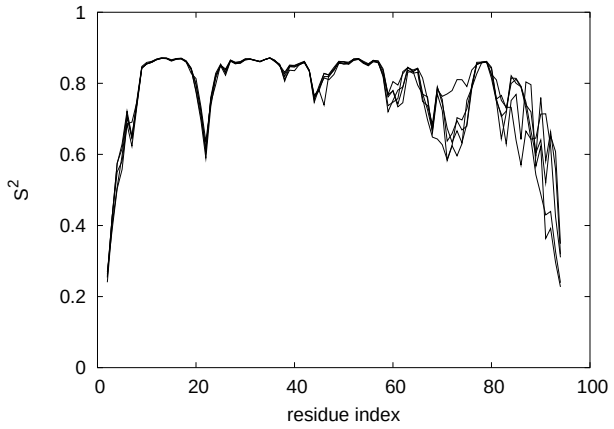

Figure 9: S^2 predictions for the first 5 NMR models of the forkhead domain of the adipocyte-transcription factor freac-11 (S12) (PDB code: 1D5V)

In the present case, residue size is much less important than local packing density and secondary structure state. The importance of local packing density agrees with the results reported by Zhang and Brueschweiler [43]. Packing density, parameterized differently, was also found to be critical in determining crystallographic B-factors [28]. The relative unimportance of residue size appears to differ from the results of Goodman and coworkers [29]. However, in that earlier study, average values of S^2 for each amino acid residue were determined first and then correlated with residue side chain volume. This procedure averages over differences in local packing density and secondary structural state and consequently accentuates the dependence on side chain volume compared to the present approach.

The Zhang-Brueschweiler formula for predicting S^2 is

$$S^2 = \tanh\left[2.656(\exp(-r_{-1}^O/1\text{Å}) + 0.8\exp(-r_0^H/1\text{Å})\right] - 0.1. \qquad (93)$$

This formula corresponds to the parametrization expression:

$$F = s_2(\mathrm{W}_2 s_1(\mathrm{W}_1 \vec{x}) + \vec{b_2}), \tag{94}$$

and can be thought of as a 2-layer perceptron with two inputs ($\exp(-r^O/1\text{Å})$ and $\exp(-r^H/1\text{Å}]$). The first layer has a transfer function is $s_1(x) = \tanh(x)$, $\mathrm{W}_1 = [2.656, 2.125]$, and no bias. The second layer has a transfer function $s_2(x)$ equal to the identity operation, $\mathrm{W}_2 = 1$, and a bias $b_2 = -0.1$. As can be seen from figure 7, a consistent improvement in prediction is obtained using the neural network model presented herein compared to the Zhang-Brueschweiler formula. Both the present model and the Zhang-Brueschweiler formula use distances to carbonyl oxygen and amide hydrogen atoms as important inputs. The improvement obtained by the neural network results in part from the different characteristic length used, 3 Åand 2 Å, for normalizing carbonyl oxygen and amide hydrogen distances, respectively, and in part from additional features in the neural network. Neither the change of the characteristic lengths, nor the addition of any single feature are responsible for most of the accuracy improvement.

Few studies of the accuracy of experimental measurements of S^2 have been reported. Difficulties in controlling for differences in the models used to fit experimental data is a confounding factor in attempts to determine absolute accuracy of experimental values of S^2 [39]; consequently, whether further improvements in prediction accuracy are limited by the quality of the experimental S^2 data or merely by the size of the feature set that can be

stably parameterized is unknown.

Conclusion

In summary, for chemical exchange, it was theoretically shown that, outside of the fast-exchange limit, NMR experiments can be used at a single magnetic field strength to extract the information about the individual sites, such as their Larmor frequencies, as well as the transition rates and the equilibrium populations. Analytical expressions with a wide range of applicability have been derived for the two-site exchange. For more than two exchanging sites, analytical expressions have been obtained for the $R_{1\rho}$ relaxation rate provided that the population of one of the sites is dominant. Moreover, it was demonstrated through simulation, that even outside of this limit, and provided that the exchange is not fast, specific information about the exchanging sites and the exchange rates can be extracted from the $R_{1\rho}$ dispersion curve.

For small-scale, picosecond to nanosecond time scale conformational fluctuations, a consistent formalism was applied to compare the statistical importance of the various features. Non-linear regression methods in the form of the artificial neural netorks were used to predict the model-free order parameters from protein structure alone. The prediction method using neural networks provided a small but consistent improvement in the prediction accuracy over the existing approaches.

One of the future directions of this research might be to apply the artificial

neural networks to the prediction of fast side-chain dynamics.

References

[1] O. Trott and A. G. Palmer. $R_{1\rho}$ relaxation outside of the fast-exchange limit. *J. Magn. Reson.*, 152:1–4, 2002.

[2] O. Trott, D. Abergel, and A. G. Palmer. An average-magnetisation analysis of $R_{1\rho}$ relaxation outside of the fast-exchange limit. *Mol. Phys.*, 101:753–763, 2003.

[3] M. Akke. NMR methods for characterizing microsecond to millisecond dynamics in recognition and catalysis. *Curr. Opin. Struct. Biol.*, 12:642–647, 2002.

[4] Dorothee Kern and Erik RP Zuiderweg. The role of dynamics in allosteric regulation. *Current Opinion in Structural Biology*, 13:748–757, 2003.

[5] J. Cavanagh, W.J. Fairbrother, A.G. Palmer, and N.J. Skelton. *Protein NMR Spectroscopy.* Academic Press, Inc., 1996.

[6] A. G. Palmer. NMR probes of molecular dynamics: Overview and comparison with other techniques. *Annu. Rev. Biophys. Biomol. Struct.*, 30:129–155, 2001.

[7] A. G. Palmer, C. D. Kroenke, and J. P. Loria. NMR methods for quantifying microsecond-to-millisecond motions in biological macromolecules. *Meth. Enzymol.*, 339:204–238, 2001.

[8] Arthur G. Palmer, Christopher D. Kroenke, and J. Patrick Loria. Nuclear magnetic resonance methods for quantifying microsecond-millisecond motions in biological macromolecules. *Meth. Enzymol.*, 339:204–238, 2001.

[9] H. M. McConnell. Reaction rates by nuclear magnetic resonance. *J. Chem. Phys.*, 28:430–431, 1958.

[10] D. G. Davis, M. E. Perlman, and R. E. London. Direct measurements of the dissociation-rate constant for inhibitor-enzyme complexes via the $T_{1\rho}$ and T_2 (CPMG) methods. *J. Magn. Reson., Ser. B*, 104:266–275, 1994.

[11] S. Meiboom. Nuclear magnetic resonance study of the proton transfer in water. *J. Chem. Phys.*, 34:375–388, 1961.

[12] R. Ishima and D. A. Torchia. Estimating the time scale of chemical-exchange of proteins from measurements of transverse relaxation rates in solution. *J. Biomol. NMR*, 15:369–372, 1999.

[13] M. Akke and A. G. Palmer. Monitoring macromolecular motions on microsecond-millisecond time scales by $R_{1\rho}$-R_1 constant-relaxation-time NMR spectroscopy. *J. Am. Chem. Soc.*, 118:911–912, 1996.

[14] J. H. Wilkinson. *The algebraic eigenvalue problem*. Clarendon Press, Oxford, 1972.

[15] A. G. Palmer. NMR characterization of the dynamics of biomacromolecules. *Chem. Rev.*, in press, 2004.

[16] K. Levenberg. A method for the solution of certain non-linear problems in least squares. *Quart. J. Appl. Math.*, 2:164–168, 1944.

[17] J. J. Moré, B. S. Garbow, and K. E. Hillstrom. User guide for MINPACK-1. Technical Report ANL-80-74, Argonne National Laboratory, Argonne, IL, USA, August 1980.

[18] E. Anderson, Z. Bai, C. Bischof, J. Demmel, J. Dongarra, J. DuCroz, A. Greenbaum, S. Hammarling, A. McKenney, and D. Sorensen. LAPACK: A portable linear algebra library for high-performance computers. Technical report, Knoxville, 1990.

[19] N. R. Skrynnikov, F. W. Dahlquist, and L. E. Kay. Reconstructing NMR spectra of "invisible" excited protein states using HSQC and HMQC experiments. *J. Am. Chem. Soc.*, 124:12352–12360, 2002.

[20] T. J. Swift and R. E. Connick. NMR-relaxation mechanisms of O^{17} in aqueous solutions of paramagnetic cations and the lifetime of water molecules in the first coordination sphere. *J. Chem. Phys.*, 37:307–320, 1962.

[21] D. M. Korzhnev, V. Yu. Orekhov, F. W. Dahlquist, and L. E. Kay. Off-resonance $R_{1\rho}$ relaxation outside of the fast exchange limit: An experimental study of a cavity mutant of T4 lysozyme. *J. Biomol. NMR*, 26:39–48, 2003.

[22] O. Millet, J. P. Loria, C. D. Kroenke, M. Pons, and A. G. Palmer. The static magnetic field dependence of chemical exchange linebroadening defines the NMR chemical shift time scale. *J. Am. Chem. Soc.*, 122:2867–2877, 2000.

[23] H. Frauenfelder, S. G. Sligar, and P. G. Wolynes. The energy landscapes and motions of proteins. *Science*, 254:1598–1603, 1991.

[24] H.A. Carlson. Protein flexibility and drug design: how to hit a moving target. *Curr. Opin. Chem. Biol.*, 6:447–452, 2002.

[25] M. Karplus. Molecular dynamics simulations of biomolecules. *Acc. Chem. Res.*, 35:321–323, 2002.

[26] D.J. Jacobs, A.J. Rader, L.A. Kuhn, and M.F. Thorpe. Protein flexibility predictions using graph theory. *Proteins: Struct., Funct., Genet.*, 44:150–165, 2001.

[27] P. Doruker, A. R. Atilgan, and I. Bahar. Dynamics of proteins predicted by molecular dynamics simulations and analytical approaches: application to a-amylase inhibitor. *Proteins: Struct., Funct., Genet.*, 40:512–524, 2000.

[28] B. Halle. Flexibility and packing in proteins. *Proc. Nat. Acad. Sci. U.S.A.*, 99:1274–1279, 2002.

[29] J. L. Goodman, M. D. Pagel, and M. J. Stone. Relationships between protein structure and dynamics from a database of NMR-derived backbone order parameters. *J. Mol. Biol.*, 295:963–978, 2000.

[30] B. R. Seavey, E. A. Farr, W. M. Westler, and J. L. Markley. A relational database for sequence-specific protein NMR data. *J. Biomol. NMR*, 1:217–236, 1991.

[31] N. A. Farrow, R. Muhandiram, A. U. Singer, S. M. Pascal, C. M. Kay, G. Gish, S. E. Shoelson, T. Pawson, J. D. Forman-Kay, and L. E. Kay. Backbone dynamics of a free and a phosphopeptide-complexed Src homology 2 domain studied by ^{15}N NMR relaxation. *Biochemistry*, 33:5984–6003, 1994.

[32] Lewis E. Kay, Dennis A. Torchia, and Ad Bax. Backbone dynamics of proteins as studied by nitrogen-15 inverse detected heteronuclear NMR spectroscopy: application to staphylococcal nuclease. *Biochemistry*, 28:8972–8979, 1989.

[33] D.R. Muhandiram, T. Yamazaki, B.D. Sykes, and L.E. Kay. Measurement of ^{2}H t_1 and $t_{1\rho}$ relaxation times in uniformly ^{13}C-labeled and fractionally ^{2}H-labeled proteins in solution. *J. Am. Chem. Soc.*, 117:11536–11544, 1995.

[34] O. Millet, D. R. Muhandiram, N. R. Skrynnikov, and L. E. Kay. Deuterium spin probes of side-chain dynamics in proteins. 1. measurement of five relaxation rates per deuteron in ^{13}C-labeled and fractionally ^{2}H-enriched proteins in solution. *J. Am. Chem. Soc.*, 124:6439–6448, 2002.

[35] G. Lipari and A. Szabo. Model-free approach to the interpretation of nuclear magnetic resonance relaxation in macromolecules. *J. Am. Chem. Soc.*, 104:4546–4570, 1982.

[36] R. Powers, G. M. Clore, D. S. Garrett, and A. M. Gronenborn. Relationships between the precision of high-resolution protein NMR structures, solution-order parameters and crystallographic B factors. *J. Magn. Reson. B*, 101:325–327, 1993.

[37] Martin C. Moncrieffe, Nenad Juranic, Marvin D. Kemple, James D. Potter, Slobodan Macura, and Franklyn G. Prendergast. Structure-fluorescence correlations in a single tryptophan mutant of carp parvalbumin: Solution structure, backbone and side-chain dynamics. *J. Mol. Biol.*, 297:147–163, 2000.

[38] A. G. Palmer, R. Hochstrasser, D. P. Millar, M. Rance, and P. E. Wright. Side chain dynamics of a zinc finger peptide characterized by ^{13}C NMR relaxation measurements and fluorescence anisotropy decay. *J. Am. Chem. Soc.*, 115:6333–6345, 1992.

[39] M. Philippopoulos, Mandel, A. M., Palmer, A. G., and C. Lim. Accuracy and precision of NMR relaxation experiments and MD simulations for characterizing protein dynamics. *Proteins: Struct., Funct., Genet.*, 28:481–93, 1997.

[40] David C. Chatfield, Attila Szabo, and Bernard R. Brooks. Molecular dynamics of staphylococcal nuclease: Comparison of simulation with ^{15}N and ^{13}C NMR relaxation data. *J. Am. Chem. Soc.*, 120:5301–5311, 1998.

[41] C.A.F Anderson, A.G. Palmer, S. Brunak, and B. Rost. Continuum secondary structure captures protein flexibility. *Structure*, 10:175–184, 2002.

[42] A. Mittermaier, A. R. Davidson, and L. E. Kay. Correlation between ^{2}H NMR side-chain order parameters and sequence conservation in globular proteins. *J. Am. Chem. Soc.*, 125:in press, 2003.

[43] F. Zhang and R. Brueschweiler. Contact model for the prediction of NMR N-H order parameters in globular proteins. *J. Am. Chem. Soc.*, 124:12654–12655, 2002.

[44] H. M. Berman, J. Westbrook, Z. Feng, G. Gilliland, T. N. Bhat, H. Weissig, I. N. Shindyalov, and P. E. Bourne. The protein data bank. *Nucleic Acids Res.*, 28:235–242, 2000.

[45] S. Hykin. *Neural networks: a comprehensive foundation*. Prentice Hall, 1999.

[46] W. Kabsch and C. Sander. How good are predictions of protein secondary structure? *FEBS Letters*, 155:179–182, 1983.

[47] M. T. Hagan and M. Menhaj. Training feedforward networks with the marquardt algorithm. *IEEE Trans. Neural Networks*, 5:989–993, 1994.